energies

MDPI

Article

An enhanced VOF method coupled with heat transfer and phase change to characterise bubble detachment in saturated pool boiling

Anastasios Georgoulas[1]*, Manolia Andredaki[1] and Marco Marengo[1]

1 Advanced Engineering Centre, School of Computing, Engineering and Mathematics, Cockcroft Building, Lewes Road, University of Brighton, Brighton, UK, BN2 4GJ; A.Georgoulas@brighton.ac.uk; M.Andredaki@brighton.ac.uk; M.Marengo@brighton.ac.uk

* Correspondence: A.Georgoulas@brighton.ac.uk; Tel.: +44-(0)1273-642900

Academic Editor: name

Received: date; Accepted: date; Published: date

Abstract: The present numerical investigation identifies quantitative effects of fundamental controlling parameters, on the detachment characteristics of isolated bubbles, in cases of pool boiling in the nucleate boiling regime. For this purpose, an improved Volume of Fluid (VOF) approach, developed previously in the general framework of OpenFOAM CFD Toolbox, is further coupled with heat transfer and phase change. The predictions of the model are quantitatively verified against an existing analytical solution and experimental data in the literature. Following the model validation, four different series of parametric numerical experiments are performed, exploring the effect of the Initial Thermal Boundary Layer (ITBL) thickness for the case of saturated pool boiling of R113 as well as the effects of surface wettability, wall superheat and gravity level for the cases of R113, R22 and R134a refrigerants. It is confirmed that the ITBL is a very important parameter in the bubble growth and detachment process. Furthermore, for all of the examined working fluids the bubble detachment characteristics seem to be significantly affected by the triple-line contact angle (i.e. the wettability of the heated plate) for equilibrium contact angles higher than 45°. As expected, the simulations revealed that the heated wall superheat is very influential for the bubble growth and detachment process. Finally, besides the novelty of the numerical approach, a last finding is the fact that the effect of gravity level variation in the bubble detachment time and volume diminishes with the increase of the ambient pressure.

Keywords: Two-phase flow, VOF method, OpenFOAM, pool boiling, phase change

PACS: J0101

1. Introduction

Boiling heat transfer is encountered in a wide field of applications, ranging from everyday life applications to more complex, industrial applications. Therefore, the exact knowledge and understanding of the boiling process and its fundamental parameters and limitations are necessary for the design and optimization of a wide range of thermal systems and technologies. Another quite important aspect regarding boiling heat transfer is the wide range of dimensional scales in the applications. For example, boiling heat transfer may be used to cool down micro-electronic components. However, boiling also occurs for example in steam generators for power plants. Due to the difficulty of generalizing the various operative conditions, boiling heat transfer has been intensively studied in the past and is still the subject of ongoing research activities in many research groups all over the world.

In spite of the ample past research, many aspects of the boiling phenomena are still not well understood. In the past, many semi-empirical correlations have been developed based on a large

number of experiments for different parameter ranges. Boiling heat convection coefficients can be estimated within these ranges with an accuracy which usually is better than ±30%, when a set of standard influencing variables are considered. However, the number of influencing parameters is very high and is further increased by new experiments deploying new experimental correlations. Therefore, in order to further improve the existing predictive tools, a deeper physical understanding of the boiling processes for the various temporal and spatial scales is necessary [1]. Generally, a comprehensive physical understanding can be achieved by either highly resolved boiling experiments and by highly resolved numerical simulations. These two approaches should not be separated or competing. They should rather be used together, in order to allow a quantitative comparison and a better capacity in designing thermal systems. In the recent years, experimental campaigns and numerical simulations have shown significant progress regarding temporal and spatial resolution as well as accuracy.

One of the earliest experimental works on boiling heat transfer was performed by Jakob and Fritz [2], where the influence of surface roughness and heat flux on the wall temperature during boiling of water was measured and reported. Later on, a theoretical approach to calculate the departure volume of bubbles as a function of the material properties of the boiling fluid and its wetting behavior on the wall was proposed by Fritz [3]. In the same period, Nukiyama [4] established the well-known pool boiling curve, publishing one of the most important papers in boiling research. In the following decades, many experimentally derived correlations have been reported in order to predict the fundamental bubble detachment diameter and frequency (e.g. [5–7]) as well as the heat transfer coefficients (e.g. [8]). All these correlations, have been mainly implemented in 1D numerical models and applied for practical engineering design calculations. However, these are valid only in the limited region of fluid properties, working conditions and geometrical configurations corresponding to the experimental databases to which they were fitted. Using larger lookup tables based on a great number of experiments, a significant range of fluid properties and working conditions can be covered. But the applicability of such modeling methods is still limited to the reference geometry for which they were developed. However, in the absence of more sophisticated predictive models, many of these physical models are still in use for the design of various technical applications. For a more detailed overview of the majority of the experimentally derived correlations, the reader may refer to the work of Carey [9].

During the last decades, the rapid advancement in the experimental technology, led to the development of modern measuring instruments and techniques that significantly increased the spatial and temporal resolutions that can be resolved by laboratory experiments. This enabled the experimental investigation of local and instantaneous quantities such as the local wall temperature underneath a vapor bubble or the instantaneous heat transfer at the bubble foot during the boiling process. In particular, the use of thermo-chromic liquid crystals (TLCs) (e.g. [10–12]), Indium-Tin-Oxide (ITO) transparent heaters in combination with high speed imaging (e.g. [13,14]), high speed infrared thermography and particle image velocimetry (e.g. [15,16]) as well as the use of micro heater arrays to impose constant temperature or constant heat flux boundary conditions (e.g. [17–20]), have offered more detailed insight regarding the transient character of boiling heat transfer. However, all these modern and high resolution techniques are still not sufficient to completely understand the microscale heat transfer in the vicinity of the three-phase contact line (liquid-vapor-solid). In particular the temperature of the liquid surrounding the vapor bubble could not yet be measured with satisfying resolution. The local wall temperature can be measured within a certain distance to the three-phase contact line, while the temperature in the liquid is measured only at certain points in the far-field. However, the use of micro-thermocouples and micro-piezoelectric pressure transducers (e.g. [21,22]) is a quite promising approach to overcome such problems.

With the growing computing capabilities and amount of available computing resources as well as with the rapid development of modern numerical methods for the simulation of multiphase flows, the numerical simulation of boiling heat transfer has become possible, for a wide range of applications as well as spatial and temporal scales. In the recent years, the use of CFD codes has been

extended to the analysis of three-dimensional, multi-phase flows, aiming to overcome the weakness of 1D numerical models.

Typically, up to present, there are two main branches in the literature for the numerical investigation of boiling heat transfer by the use of CFD.

In the first branch, most of the existing open-source, in-house, and especially commercial CFD codes have adopted a Eulerian multiphase flow approach, based on a two-fluid model. With this approach, governing equations for mass, momentum and energy are solved for each phase, separately, weighted by the so-called Volume Fraction, which represents the ensemble averaged probability of occurrence for each phase at a certain point in time and space. Interaction/exchange terms between the phases appear as source/sink terms in the governing equations. These exchange terms normally consist of analytical or empirical correlations, expressing the interfacial forces, as well as heat and mass fluxes, as functions of the average flow parameters. However, most of these correlations are highly problem-specific and therefore their applicability and validity range must be carefully considered. Moreover, for the case of boiling flows, where heat is transferred into the fluid from a heated wall, additional source terms accounting for the underlined physics of these processes at the wall, have to be included. For this purpose these global multi-phase CFD models are usually coupled with appropriate wall boiling sub-models, like the most widely used *wall partitioning model* of Kurul and Podowski [23]. Some representative and relatively recent numerical investigations in this branch are the works by Steiner et al. [24] , Koncar and Krepper [25], Lopez-de-Bertodano et al. [26], Yun et al. [27], and Krepper et al. [28]. Conversely, such wall boiling sub-models require additional closure relationships to predict for example the bubble departure characteristics and the density of the active nucleation sizes, incorporating a number of model constants, the value of which can be found only for specific flow conditions and working fluids. Recently, in the work of Prabhudharwadkar et al. [29] and Cheung et al. [30], the performance of a wide combination range of the existing closure relationships is examined through comparison with a wide range of experimental data. It is stated that no single combination of empirical correlations provides satisfactory predictions covering the entire range of the simulated conditions.

In the second branch, a complete or "direct" numerical simulation of the complex spatial and temporal evolution of the interface between the two phases is followed. The most widely used methods in this direction are Marker and Cell (MAC) method [31], the Front Tracking (FT) method [32], the Arbitrary Lagrangian-Eulerian (ALE) method [33], the Volume-of-Fluid (VOF) method [34] and the Level-Set (LS) method [35].

One of the first boiling simulations, based on the MAC method, was conducted in the work of Madhaven et al. [36]. The originally developed FT method [37] has been further modified by Unverdi and Tryggvason [38] and Tryggvason et al. [32] for the simulation of boiling heat transfer. The method showed very accurate predictions especially in the calculation of the liquid-vapor interface curvature, which is vital for the simulation of boiling flows. However the FT method was mainly used for the simulation of film boiling ([39–42]).

A quite similar numerical method to ALE for the simulation of two-phase flows with phase change, was firstly applied by Welch ([43,44]). The latest ALE method [33] was applied by Fuchs et al. [45], in order to simulate the transient characteristics in pool boiling of binary mixtures. Fuchs, was based on the work by Kern and Stephan ([46,47]), where the heat flow at a growing bubble was calculated by utilizing a boundary-fitted mesh. One important aspect of boundary-fitted meshes is the possibility to treat the liquid-vapor interface as a boundary of the computational domain. This facilitates the estimation of the heat flux at the interface and therefore of the evaporation rate.

The VOF method can be considered as the most popular interface capturing approach and it has been also used so far, for the simulation of boiling flows. Welch and Wilson [48] implemented a phase change model in a VOF method and simulated 1D test cases and film boiling. Welch and Rachidi [49] extended the model by the transient heat conduction in the solid wall and simulated film boiling. Aus der Wiesche [50] used the VOF method to simulate nucleate pool boiling of water. Hardt and Wondra [51] have proposed a method for implementing phase change in a VOF or LS approach and performed simulations of film boiling and droplet evaporation, using a VOF method. Kunugi et al.

147 [52] simulated sub-cooled pool and flow-boiling problem by the MARS code and Ose and Kunugi in
148 their works ([53,54]) conducted sub-cooled pool boiling simulations and validated the numerical
149 results by their own visualization experimental data. Some more recent works on boiling simulation
150 based on the VOF methods have also been reported ([55,56]). However, none of the aforementioned
151 models based on the VOF method, include any sub-model for evaporation at the 3-phase contact line.
152 In this sense, Kunkelmann et al. [57] implemented a specific sub-model in the VOF solver of the open-
153 source CFD package OpenFOAM [58], that solves incompressible two-phase flow problems. Detailed
154 information on the proposed numerical method can be also found in Kunkelmann's PhD thesis [59].
155 Already in the late 1990s, Son and Dhir [60] numerically investigated film boiling and then Son
156 et al. [61] investigated the heat transfer associated with a single bubble during nucleate pool boiling,
157 by application of the LS method. In the same decade, a lot of works have also been conducted by Dhir
158 and co-workers for a variety of boiling flows, summarized by Dhir [62]. A considerable number of
159 more recent works on boiling heat transfer have also been published that utilize the LS method for
160 boiling heat transfer numerical investigations (e.g [63]). The advantages of the VOF and LS methods
161 have in many cases been combined in order to be applied for the simulation of boiling heat transfer
162 related problems. This combined method is known as CLSVOF (Combined Level Set and Volume Of
163 Fluid). For example, Shu [64] in his PhD thesis, applied the CLSVOF method to simulate boiling heat
164 transfer using the open-source CFD package OpenFOAM, performing 2D simulations, stating that
165 the extension of the model to 3D simulations was straightforward. Apart from the aforementioned
166 methods, other different approaches like the Lattice Boltzmann method [65] and the Phase Field
167 method [66] have been also applied for the simulation of boiling heat transfer.
168 In the present investigation, an enhanced VOF-based numerical model that utilises a smoothing
169 technique in order to suppress the development of spurious velocities in the vicinity of the interface
170 that was previously presented, validated and applied to the investigation of adiabatic bubble
171 dynamics in the work of Georgoulas et al. [67], is further extended for the simulation of diabatic,
172 liquid-vapour flows with phase change. In more detail, an energy transport equation and the phase
173 change model, originally proposed by Hardt and Wondra [51], are implemented to a previously
174 improved and validated (against experimental data) adiabatic, VOF solver of OpenFOAM. The
175 proposed phase change model [51] has been also utilised in previous similar investigations (e.g.
176 [58,59,68]). The model is initially verified against an analytical solution for a bubble evaporating in a
177 superheated liquid, for three different working fluids with a very good degree of agreement. Apart
178 from this, the predictions of the proposed model regarding the bubble detachment diameter and time
179 are also validated against literature available experimental results of pool boiling of refrigerants [69].
180 Then, the validated and optimised version of the model is further applied for the conduction of a
181 wide range of parametric numerical experiments, identifying the effects of the Initial Thermal
182 Boundary Layer (ITBL) thickness, the surface wettability (triple-line contact angle), the plate
183 superheat and the gravity level, on the bubble detachment characteristics.

184 **2. Numerical Method**

185 *2.1. Governing Equations*

186 In this section, the governing equations for mass, momentum, energy, and volume fraction are
187 presented. It should be mentioned that liquid and vapour phases are both treated as incompressible,
188 Newtonian fluids. The mass conservation equation is given as:

$$\nabla \cdot \left(\rho \vec{U}\right) = \dot{\rho}, \tag{1}$$

189

190 where U is the fluid velocity and ϱ is the bulk density. The source term on the right hand side accounts
191 for the phase change. It should be mentioned that despite of the local source terms the mass is globally
192 conserved since all of the mass that is removed from the liquid side of the interface is added on the
193 vapour side.

194 The conservation of momentum is given by the following equation:

$$\frac{\partial}{\partial t}\left(\rho\vec{U}\right) + \nabla\cdot\left(\vec{U}\cdot\rho\vec{U}\right) = -\nabla \mathrm{p} + \nabla\cdot\left(\mu\nabla\vec{U}\right) + \vec{f}_{ST} + \vec{f}_{g}, \quad (2)$$

195

196 where p is the pressure and μ is the bulk dynamic viscosity. The momentum source terms in the right
197 hand side of the equation account for the effects of surface tension and gravity, respectively. The
198 surface tension term is modelled according to the classical approach of Brackbill et al. [70].

199 The conservation of energy balance is given by the following equation:

200

$$\frac{\partial}{\partial t}\left(\rho c_p T\right) + \nabla\cdot\left(\vec{U}\cdot\rho c_p T\right) = \nabla\cdot\left(\lambda\nabla T\right) + \dot{h}, \quad (3)$$

201

202 where c_P is the bulk heat capacity, T the temperature field, and λ is the bulk thermal conductivity.
203 The source term on the right hand side of the equation represents the latent heat of evaporation.

204 The volume fraction α is advected by the flow field by the following equation:

$$\frac{\partial\alpha}{\partial t} + \nabla\cdot\left(\alpha\vec{U}\right) - \nabla\cdot\left(\alpha(1-\alpha)U_r\right) = \frac{\dot{\rho}}{\rho}\alpha, \quad (4)$$

205
206 Interface sharpening is very important in simulating two-phase flows of two immiscible fluids.
207 In OpenFOAM the sharpening of the interface is achieved artificially by introducing the extra
208 compression term in Equation 4 ($\nabla\cdot(\alpha(1-\alpha)U_r)$). U_r is the artificial compression velocity which is
209 calculated from the following relationship:
210

$$U_r = n_f min\left[C_\gamma\frac{|\varphi|}{|S_f|}, max\left(\frac{|\varphi|}{|S_f|}\right)\right], \quad (5)$$

211
212 where n_f is the cell surface normal vector, φ is the mass flux, S_f is the surface area of the cell, and C_γ
213 is a coefficient the value of witch can be set between 1 and 4. U_r is the relative velocity between the
214 two fluid phases due to the density and viscosity change across the interface. In Equation (4) the
215 divergence of the compression velocity U_r, ensures the conservation of the volume fraction α, while
216 the term $\alpha(1\text{-}\alpha)$ limits this artificial compression approach only in the vicinity of the interface, where
217 $0 < \alpha < 1$ [71]. The level of compression depends on the value of C_γ ([71,72]). For the simulations of the
218 present investigation, initial, trial simulations indicated that a value of $C_\gamma = 1$ should be used, in order
219 to maintain a quite sharp interface without at the same time having unphysical results. The source
220 term on the right hand side of the Equation 4 is needed because, due to the local mass source terms,
221 the velocity field is not free of divergence.
222 It should be mentioned that the VOF method in OpenFOAM does not solve Equation 4
223 implicitly, but instead applying a multidimensional universal limiter with explicit solution algorithm
224 (MULES). Together with the interface compression algorithm, this method ensures a sharp interface
225 and bounds the volume fraction values between 0 and 1 [73].
226 Finally, the bulk fluid properties γ are computed as the averages over the liquid (γ_l) and vapour
227 (γ_v) phases, weighted with the volume fraction α:
228

$$\gamma = \alpha\gamma_l + (1-\alpha)\gamma_v, \quad (6)$$

As it is known, the VOF method usually suffers from non-physical spurious currents in the interface region. These spurious velocities are due to errors in the calculation of the normal vectors and the curvature of the interface that are used for the calculation of the interfacial forces. These errors emerge from the fact that in the VOF method the interface is implicitly represented by the volume fraction values that encounter sharp changes over a thin region [74].

As previously mentioned in the introduction section of the present paper, the VOF-based solver that is used in the present investigation has been modified accordingly in order to account for an adequate level of spurious currents suppression. The proposed modification involves the calculation of the interface curvature κ using smoothed volume fraction values $\tilde{\alpha}$ that are obtained from the initially calculated volume fraction field α, smoothing it over a finite region in the vicinity of the interface:

$$\kappa = \nabla \cdot \left(\frac{\nabla\tilde{\alpha}}{|\nabla\tilde{\alpha}|}\right), \quad (7)$$

All other equations are using the initially calculated (non-smoothed) volume fraction values of α. The proposed smoothing is achieved by the application of a Laplacian filter which can be described by the following equation:

$$\tilde{\alpha}_p = \frac{\sum \alpha_f S_f}{\sum S_f}, \quad (8)$$

In Equation 8, the subscripts P and f denote the cell and face index respectively and α_f is the linearly interpolated value of α at the face center. The application of the proposed filter can be repeated more than one time in order to obtain an adequately smoothed field. For the applications of the present investigation, initial trial simulations indicated that the filter should applied no more than 2 times, in order to avoid the leveling out of high curvature regions. The proposed, enhanced VOF solver has been tested and verified against literature available experimental results in isothermal bubble dynamics with an excellent degree of convergence. More details on the proposed validation as well as on the proposed improved VOF method can be found in the paper by Georgoulas et al. [67].

2.2. Phase Change Model

The utilized phase change model that was implemented in the improved OpenFOAM VOF solver that is used in the present investigation, will be described briefly in this section. Supplementary details can be found in the work of Hardt and Wondra [51].

The evaporating mass flux at the liquid–vapour interface j_{evap} is calculated from the following equation:

$$j_{evap} = \frac{T_{int} - T_{sat}}{R_{int} h_{lv}}, \quad (9)$$

where T_{int} is the temperature of the interface, T_{sat} is the saturation temperature, R_{int} is the interfacial heat resistance and h_{lv} is the latent heat of evaporation at the saturation temperature.

The interfacial heat resistance is calculated by the following equation based in the considerations of Schrage [75],

$$R_{int} = \frac{2-\gamma}{\gamma}\frac{\sqrt{2\pi R_{gas}}}{h_{lv}^2}\frac{T_{sat}^{3/2}}{\rho_v}, \quad (10)$$

It is clear that this last equation is in fact a fitting function, due to the uncertainty of the parameter γ, which is eventually may vary in the range $0< \gamma< 1$. For the cases that will be presented here, the constant γ that is also known as the evaporation/condensation coefficient is taken equal to unity from the literature ([57–59], [76–78]). R_{gas} is the specific gas constant of the working fluid that is calculated from the universal gas constant and the molecular weight of the working fluid. The amount of liquid that evaporates is calculated locally and the resulting source term field is smeared over a few cells in order to avoid numerical instabilities. The evaporating mass is taken away on the liquid side of the interface and reappears on the vapour side. According to previous investigations ([57–59], [76–78]), despite the fact that Eqs. (9) and (10) are derived from considerations on length scales which are several orders smaller than the typical grid size used in the simulations, the proposed evaporation model leads to correct evaporation rates since it acts like a control loop. The more the temperature at the interface deviates from the saturation value, the more liquid evaporates and the more the temperature drops locally. This ensures that the temperature at the liquid–vapour interface always remains close to the saturation temperature.

The evaporating/condensing mass flux is calculated from Eq. (9) and must be incorporated into the conservation equations, by the definition of volumetric source terms. This is done by multiplying the evaporating mass flux at the liquid–vapour interface by the magnitude of the volume fraction gradient, as indicated in the following equation:

$$\dot{\rho}_0 = j_{evap}|\nabla a|, \quad (11)$$

This initial *sharp source term field* (SSTF) is integrated over the whole computational domain to calculate the "Net Mass Flow" through the entire liquid-vapour interface, using the following equation:

$$\dot{m}_{int} = \iiint \dot{\rho}_0 dV, \quad (12)$$

This value is important for the global mass conservation, in order to ensure that the magnitudes of the mass sources in the liquid and vapour parts are equal and correspond to the net evaporation rate. The sharp source term field is then smeared over several cells, by solving the following diffusion equation for the smooth distribution of source terms

$$\dot{\rho}_1 - \nabla \cdot [(D\Delta\tau)\nabla\dot{\rho}_1] = \dot{\rho}_0, \quad (13)$$

$\Delta\tau$ is an artificial time step and Neumann boundary conditions are imposed for the smooth source term field on all boundaries of the domain. Therefore, the integral values of the sharp and the smooth source fields remain the same, in spite of the smearing. The width of the smeared source term field is proportional to the square root of the product of the diffusion constant "D" and the artificial time step "$\Delta\tau$". It should be mentioned that the value of "D" must be adjusted to the mesh resolution such that the source term field is smeared over several cells.

Then, the source terms in all cells that do not contain pure liquid or vapour ($\alpha < 1\text{-}\alpha_{cut}$ and $\alpha > \alpha_{cut}$, where α_{cut} may be set to 0.05) are artificially set to zero. This cropping step ensures that source terms are shifted into the pure vapour and liquid cells only in the vicinity of the interface. The interface therefore is not subjected to any source terms and is only transported by the calculated velocity field. Therefore, the transport algorithm for the volume fraction field as well as the associated interface compression, can work efficiently without any interference with the source term field. The

remaining source term field is scaled individually on the liquid and the vapour side through the application of appropriate scaling coefficients. This scaling step ensures that the mass is globally conserved and that the evaporating or condensing mass flow, corresponds globally to the net mass flow through the interface.

The newly proposed scaling coefficients N_l and N_v are calculated by integrating the smooth source term field in each of the pure phases and comparing it to the net mass flow $\dot{m}_{int}$ (Equation 12), utilizing the following equations:

$$N_l = \dot{m}_{int}[\iiint (\alpha - 1 + a_{cut})\, \dot{\rho}_1 dV]^{-1}, \quad (14)$$

$$N_v = \dot{m}_{int}[\iiint (a_{cut} - \alpha)\, \dot{\rho}_1 dV]^{-1}, \quad (15)$$

Finally, the final source term distribution is calculated using the above scaling factors in the following equation:

$$\dot{\boldsymbol{\rho}} = \boldsymbol{N_v(\alpha_{cut} - \alpha)\dot{\rho}_1 - N_l(\alpha - 1 + \alpha_{cut})\dot{\rho}_1}, \quad (16)$$

An example of the aforementioned final source term distribution is depicted indicatively in Fig. 1 below.

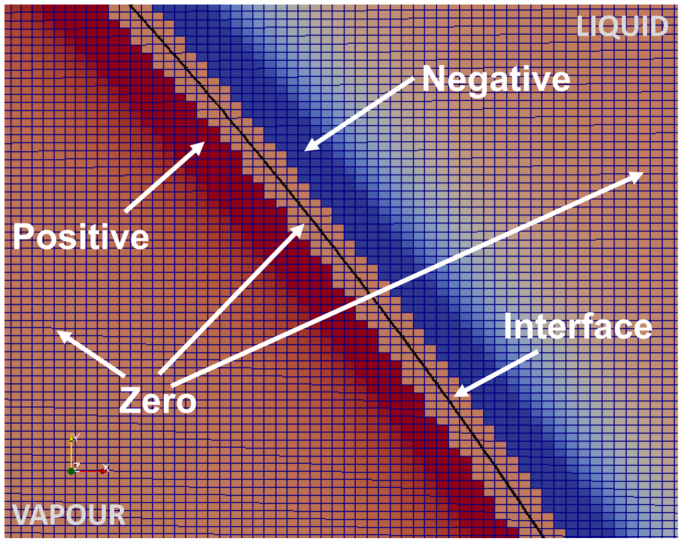

Figure 1. Distribution of the final source terms in the computational domain for the case of an evaporating bubble.

2.3 Simulation Parameters

As mentioned previously, all the numerical simulations on pool boiling of the present work were performed with the finite-volume-based CFD code OpenFOAM (version 2.2.1) utilizing and enhancing its original VOF-based solver "interFoam". For pressure–velocity coupling, the PISO (Pressure-Implicit with Splitting of Operators) scheme is applied. The transient terms in the equations are discretized using a second order, bounded, implicit scheme (Euler). The calculation time step is controlled by setting the maximum Courant number to 0.2. With this adaptive time stepping technique, the time step is automatically varied from approximately 10^{-9} to 10^{-6} sec, for the overall simulation cases that are presented in the present paper. The gradient terms are discretized using a

second order, Gaussian integration with linear interpolation (Gauss linear). For the divergence terms different discretisation schemes are applied for each term in the equations. In more detail the convection term of Eq. (2) is discretised using a "Gauss upwind" scheme. The $\nabla \cdot \left(\alpha \vec{U}\right)$ term of Eq. (4) is discretised using the "Gauss vanLeer" scheme, while the $\nabla \cdot (\alpha(1-\alpha)U_r)$ term is discretised using the "Gauss interfaceCompression" scheme that ensures the boundedness of the calculated volume fraction field. Finally, all Laplacian terms are discretised using the "Gauss Linear Corrected" scheme. The divergence term of Eq. (3) is discretised using a "Gauss linear" scheme. Further details regarding the adopted discretization schemes can be found in OpenFOAM Documentation (OpenFOAM, 2013 [73]). It should be mentioned that this was the optimum combination of discretization schemes in order to maintain a balance between accuracy, convergence and numerical stability during the computations.

3. Validation of Numerical Method

3.1 Growth of a Spherical Bubble in a Superheated Liquid

The first test case that was selected in order to validate the previously described implementations in the improved VOF-based numerical model, is the growth of a spherical bubble in an infinitely extended superheated liquid domain. This test case constitutes a widely used test case for the validation of boiling models throughout the literature (e.g. [51], [58], [68], [78–80]).

The growth of the bubble within a superheated liquid domain follows two distinct stages. At the initial stage the bubble growth is mainly controlled by the effects of surface tension and inertia. At the second stage, the growth is controlled only by the heat transfer rate from the superheated liquid to the liquid–vapour interface. During this final stage, it can be assumed that the bulk vapour and the liquid–vapour interface are at saturation temperature. More details regarding the simulated phenomenon are described in detail in the work of Plesset and Zwick [79]. An analytical solution for this situation has been derived by Scriven [80]. According to this analytical solution the bubble radius as a function of time is given by the following equation:

$$R(t) = 2\beta\sqrt{Dt}, \tag{17}$$

where β is a growth constant, details of which can be found in the work of Scriven [80], and D is the thermal diffusivity of the liquid. This analytical solution permits the calculation of the initial conditions for the numerical simulations (initial temperature profile at the bubble interface and initial bubble radius), in order to validate the numerical results. Here, all the details for the initial conditions of the simulations that are going to be presented, are taken from the works of Kunkelmann and Stefan [58] and Magnini [78], which were derived from the above mentioned analytical solution [80] for the time instant that the bubble in each case has a radius of 0.1 mm. The geometric characteristics and the initial conditions of the considered physical problem are illustrated schematically in Fig. 2.

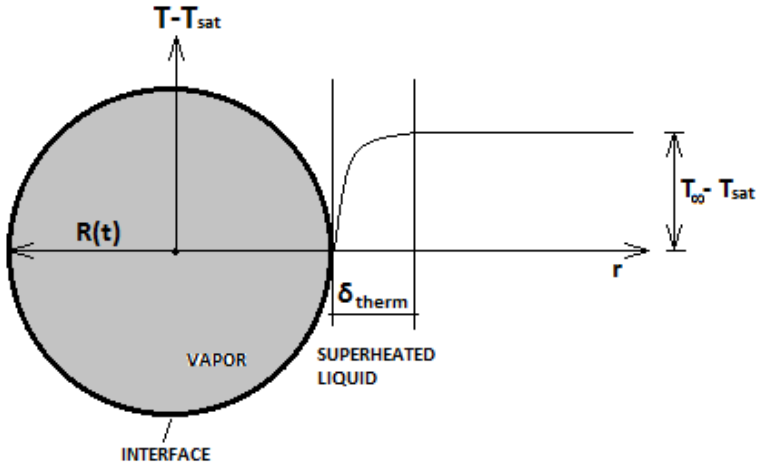

Figure 2. Schematic illustration of the geometrical characteristics and the initial conditions of the simulated validation cases.

2D axisymmetric simulations were performed for three different working fluids, Water and FC-72 liquid at equilibrium with their corresponding vapour phases (saturation point), at a pressure value of 1013 mbar, as well as R134a liquid at equilibrium with its vapour phase at a pressure value of 840 mbar. Uniform hexahedral grids of 1μm cell dimension were used in all three cases. The computational domain and grid that was constructed as well as the applied boundary conditions are depicted in Fig. 3. The initial conditions for the Water liquid/vapour case are illustrated in Fig. 4, while the material properties and the initial conditions for all fluid cases are summarised in Table 1.

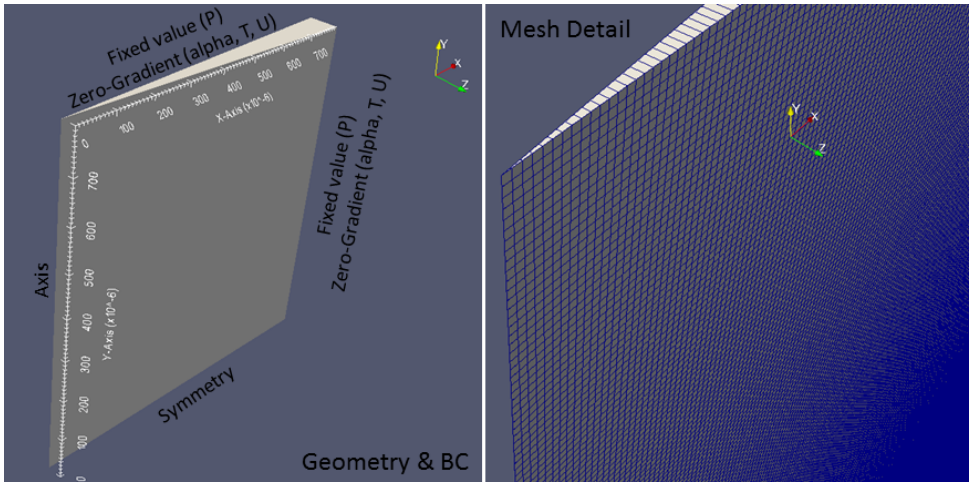

Figure 3. 2D-axisymetric computational domain, mesh and boundary conditions.

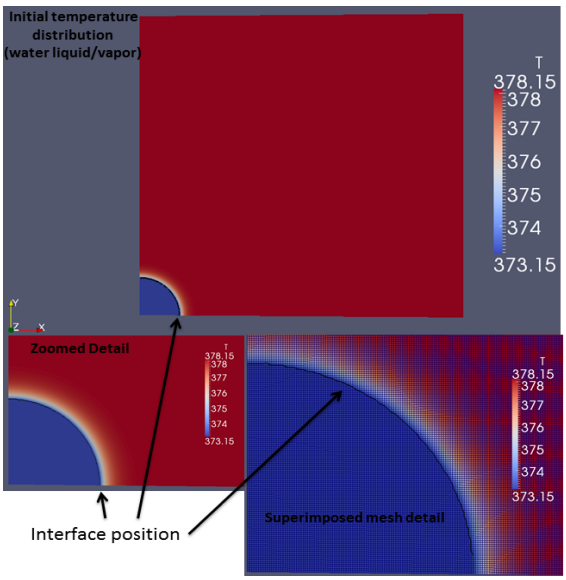

388

389 **Figure 4.** Initial conditions for the water liquid/vapour: P= 1.013bar, 5K of liquid superheat.

390 **Table 1.** Material properties and initial conditions for the numerical simulations (validation cases).

Property	Unit	Water		R134a		FC-72	
		Liquid	Vapour	Liquid	Vapour	Liquid	Vapour
Density ϱ	(kg/m^3)	958	0.597	1388	4.43	1621.2	13.491
Specific heat capacity c_p	(J/kg.K)	4220	2030	1270	720	1106.7	924.81
Thermal conductivity k	(W/m.K)	0.679	0.025	0.106	0.009	0.054165	0.013778
Dynamic viscosity μ	(Pa.s)	2.77x10^{-4}	1.30x10^{-5}	4.01x10^{-4}	9.64x10^{-6}	4.13x10^{-4}	1.19x10^{-5}
Heat of vaporization h_{lv}	(J/kg)	2257000		219500		83562	
Surface tension σ	(N/m)	0.059		0.016		0.0084	
Saturation temperature T_{sat}	(K)	373.15		303.15		330.06	
Pressure P	(bar)	1.013		0.84		1.013	
Growth constant β	(-)	14.59		8.75		7.69	
Initial thermal layer thickness δ_{therm}	m	7.00x10^{-6}		1.10x10^{-5}		1.30x10^{-5}	
Thermal diffusivity D	(m^2/s)	1.68x10^{-7}		6.01x10^{-8}		3.02x10^{-8}	
Superheat ΔT	(K)	5		5		5	

391

Finally, in Fig. 5, the spatial and temporal evolution of the numerically predicted bubble growth is illustrated through the resulted temperature field, at each time instant of the simulation for the Water liquid/vapour case, while in Fig. 6 a quantitative comparison of the numerical predictions with the analytical solution is conducted for all fluid cases.

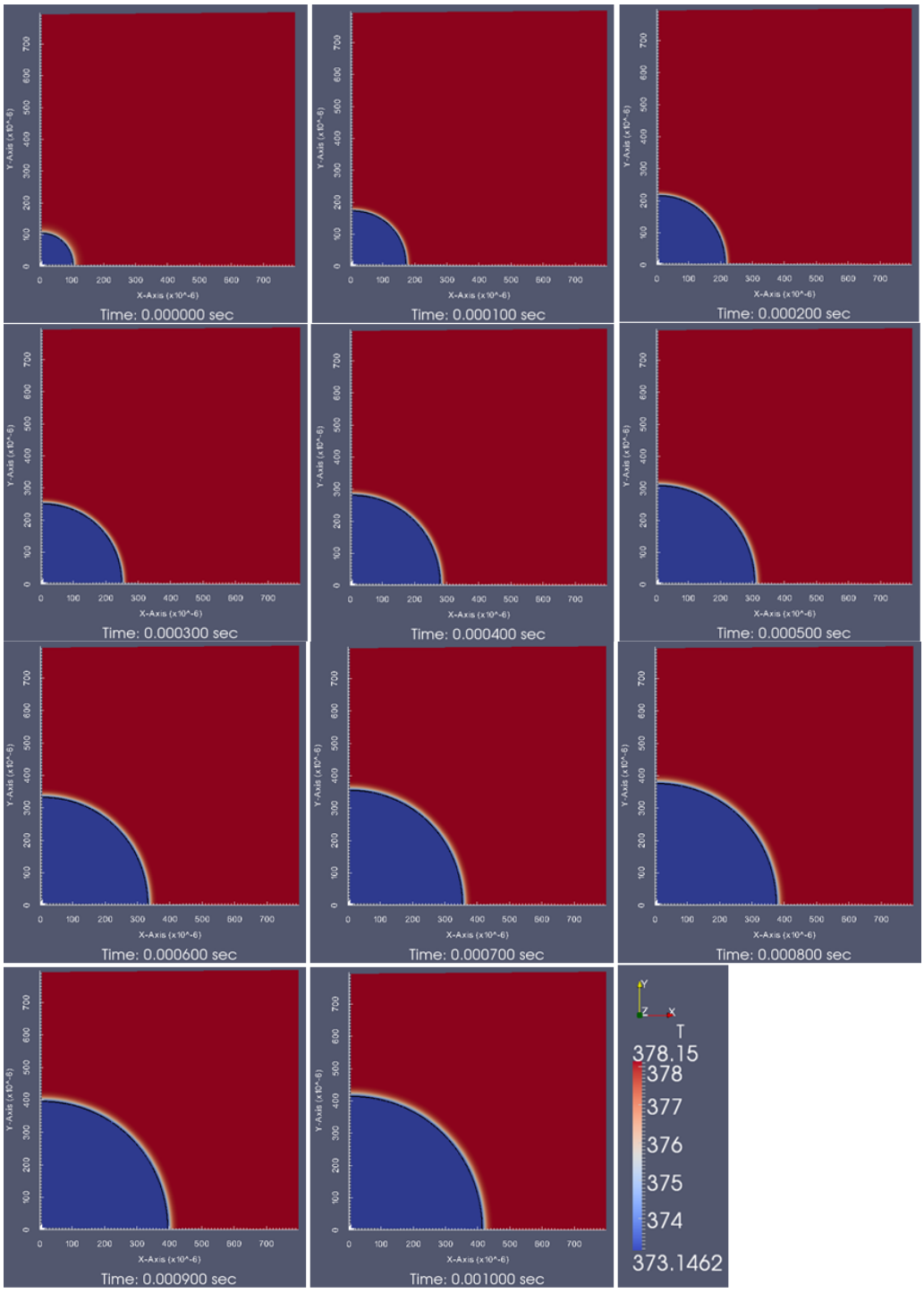

Figure 5. Bubble evolution with time for the Water Liquid/Vapour simulation (P= 1.013 bar, ΔT = 5K).

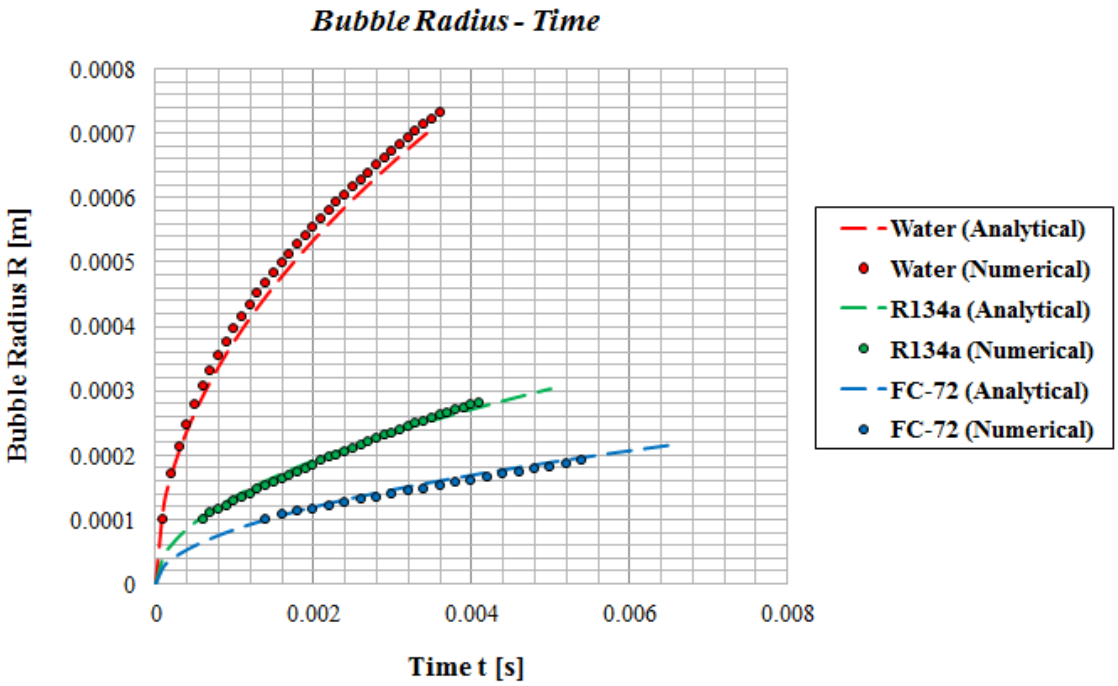

400

401 **Figure 6.** Bubble Radius with respect to time for three different fluid cases. Comparison of numerical
402 (present investigation) and analytical predictions [80].

403 As it can be observed the developed numerical model of the present paper adequately predicts the
404 vapour bubble growth within the superheated liquid domain, for all of the considered fluid cases, in
405 comparison with the proposed analytical solution [80].

406

407 *3.2 Pool Boiling*

408 3.2.1. Problem Definition

409 In order to further validate the numerical model, the experiments on single bubble growth in
410 saturated pool boiling on a constant wall temperature boundary condition, reported in the work of
411 Lee et al. [69], were selected among others, since many necessary data used for their numerical
412 reproduction are accurately reported by the authors. In more detail, in the proposed work nucleate
413 pool boiling experiments with constant wall temperatures were performed using R11 and R113
414 refrigerants, for various saturated conditions. A micro-scale heater array and Wheatstone bridge
415 circuits were used to maintain a constant wall temperature condition and to obtain measurements
416 with high temporal and spatial resolution. Accurate heat flow rate data were obtained from the
417 micro-scale heater array by controlling the surface conditions at a high temporal resolution. Images
418 of the bubble growth were captured using a high-speed CCD camera synchronised with the heat flow
419 rate measurements. The geometry of the bubble was obtained from the images. In the present paper,
420 one specific experimental run for R113 is reproduced numerically and presented as a validation case.
421

422 3.2.2. Computational set-up

423 Since, the processes of bubble growth and detachment in the proposed experiment can be
424 considered to be axisymmetric, an axisymmetric computational domain was constructed for its
425 numerical reproduction. The adopted computational domain, mesh and boundary conditions are
426 illustrated in Fig. 7. As it can be seen, a wedge type geometry was constructed representing a 5^{o}
427 section of the corresponding 3D domain in the considered physical problem. A non-uniform

structured computational mesh with local refinement was used consisting of 400,000 hexahedral cells. A minimum cell size of 2μm and a maximum cell size of 4μm were selected in the bottom left and top right corners of the computational domain respectively, in order for the solution to be mesh-independent. The overall domain size in the XY plane is 2.5 mm x 4 mm. These dimensions were indicated from initial, trial simulations that were conducted in order to determine the minimum distances between the axis of symmetry and the side wall boundary (domain width) as well as between the bottom wall and the outlet (domain height), in order to avoid any influence of these boundaries in the computed bubble growth and detachment process.

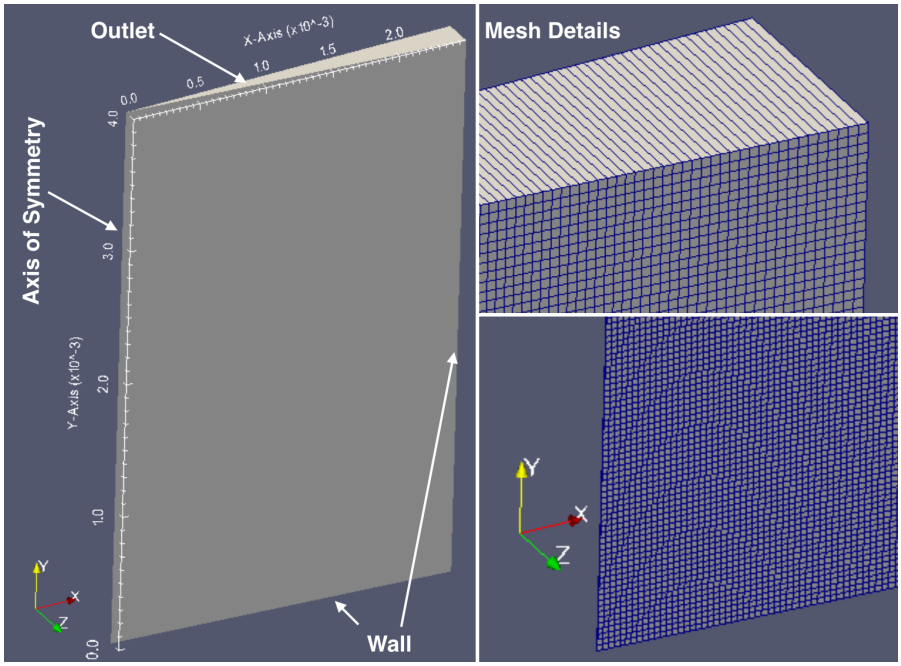

Figure 7. Computational domain, mesh and boundary conditions.

At the solid walls, a no-slip velocity boundary condition was used with a fixed flux pressure boundary condition for the pressure values. At the lower wall, a constant contact angle of $\theta=30^{o}$ is imposed for the volume fraction field. According to Lee et al. [69], the static equilibrium contact angle of the micro-scale heater array surface was 11.4^{o} for R113. However, the dynamic characteristics of a boiling bubble are supposed to be different with respect to the static equilibrium contact angle, which is usually measured with the sessile drop method, and at ambient temperature and pressure conditions. Therefore, the value of $\theta=30^{o}$ that was finally selected for the numerical simulation, was chosen after a series of parametric numerical simulations, where contact angles ranging from 11.4^{o} to 160^{o} were tested. The adopted value of $\theta=30^{o}$ indicated closest numerical predictions to the corresponding experimental observations. The proposed parametric analysis is presented in detail in the following section 4.2. For the side wall, a zero gradient boundary condition was used for the volume fraction values. As for the temperature field, a constant temperature of $T_w=334.15$ K (in accordance to the selected experimental run) was imposed in the bottom wall and a zero gradient boundary condition was used for the sidewall. At the outlet, a fixed-valued pressure boundary condition and a zero-gradient boundary condition for the volume fraction were used, while for the velocity values a special (combined) type of boundary condition was used that applies a zero-gradient when the fluid mixture exits the computational domain and a fixed value condition to the tangential velocity component, in cases that fluid enters the domain. Finally, a zero gradient boundary condition for the temperature field was also prescribed at the outlet boundary. The fluid properties the initial conditions as well as some computational details for the simulation imitating the selected experimental run are summarised in Table 2.

Table 2. Fluid properties and initial conditions.

		ρ (kg/m³)	c_p (J/kgK)	k (W/mK)	ν (m²/s)	σ (N/m)	h_{lv} (J/kg)
Phase properties (R113 at 1bar, T_{sat} = 320.65K)	Liquid	1508.4	940.3	0.064	3.25×10^{-7}	0.015	144350
	Vapour	7.4	691.3	0.0095	1.39×10^{-6}		
Initial Conditions	Initial bubble (seed) radius: 50 μm		ΔT = 13.5K		Domain size (mm): 2.5x4.0		
			Contact angle: 30°				
	Initially developed thermal boundary layer thickness: 352 μm		Simulation Type: axisymmetric		No. of computational cells: 400000		

The initial temperature of R113 liquid in the computational domain is assumed to be at saturation temperature. Then a single-phase transient solution is started for a certain time period in order for the initial temperature boundary layer to be developed in the vicinity of the heated wall. After the development of a desired temperature boundary layer thickness, an initial seed bubble of 50μm in radius is patched at the bottom wall, as a 5° section of a hemisphere (axisymmetric simulation), which immediately starts to evaporate. The initial condition for the two-phase simulation corresponds to the time when the bubble seed is planted in the domain (Fig. 8).

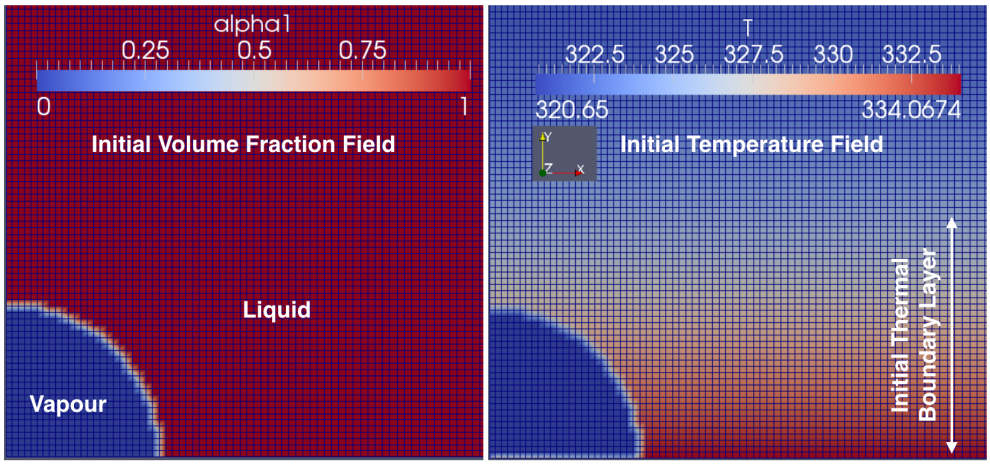

Figure 8. Initial conditions for the simulation.

At this point it should be mentioned that, since the initial thermal boundary layer thickness was not measured in the experiments of Lee et al. [69], a series of parametric numerical simulations was performed, utilising a wide number of successive thicknesses, developed in the single-phase simulation, at successive time instances. More details regarding the effect of the initially developed boundary layer characteristics on the bubble growth and detachment process are given in section 4.1. A thickness of 352μm, which corresponds to a development time of 0.08s, showed the best match with the corresponding experimental results.

3.2.3 Comparison of numerical and experimental results

In Fig. 9, the reconstructed 3D evolution of the 0.5 volume fraction contour (interface) from the axisymmetric simulation is compared with the corresponding experimental snapshots, for approximately the same time instances that correspond to the bubble detachment stage, while in

Table 3 the numerically predicted bubble detachment characteristics are compared with the corresponding experimental values.

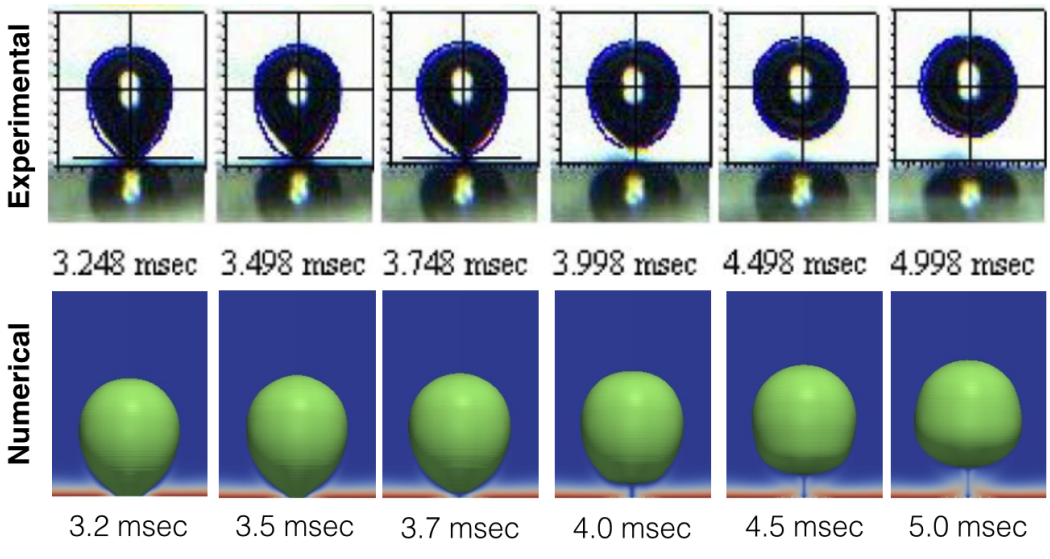

Figure 9. Qualitative comparison of experimental [69] and numerical (present investigation) 3D bubble evolution.

As it can be observed the numerical model predictions are in very good agreement with the corresponding experimental data. The numerically predicted spatial and temporal evolution of the generated bubble matches very well with the corresponding experimental images (Fig. 9). Some small deviations in the shape of the bubble especially after its detachment from the heated plate can be attributed to the fact that the proposed experimental images were recorded after a few bubble cycles, while the numerical simulation images represent the first bubble cycle. However, as it is indicated in Table 3, the numerical model predictions regarding the bubble detachment time and the equivalent bubble detachment diameter, are in very close agreement with the corresponding experimental values.

Table 3. Predicted (present investigation) and measured [69], bubble detachment characteristics.

	Bubble detachment time (msec)	**Equivalent bubble detachment diameter (mm)**
Experimental [69]	3.748	0.704
Numerical (present investigation)	3.700	0.740
% Error	1.28	5.11

4. Application of the Validated Numerical Model for the Simulation of Pool Boiling Characteristics

In the current section of the present work, the validated numerical model is further applied for the conduction of four different series of parametric numerical simulations, aiming to identify and quantify the effects of fundamental controlling parameters in the bubble growth and detachment characteristics, identified as being important during the validation process.

In more detail, the first series (Series-A) aims to identify the effect of the initial thermal boundary layer, the second (Series-B) the effect of the triple line contact angle (wettability), the third (Series-C) the effect of wall superheat and the fourth (Series-D) the effect of the gravity level, in the bubble growth and detachment characteristics.

In all these simulations, the same computational domain, mesh and boundary conditions with the validation case presented in the previous section is used. Three different refrigerants were used as working fluids. R113, as in the validation section of the present paper, is used for Series A, while R113 as well as R22 and R134a, are used for the numerical simulations of Series B, C and D, since these are among the most widely used working fluids in boiling applications. The corresponding fluid properties and initial conditions for the base cases that are used as reference in the proposed series of parametric numerical simulations, are summarized in Tables 4, 5 and 6, respectively.

Table 4. Fluid properties and initial conditions (Base case for R113 refrigerant, Series A, B, C and D).

<table>
<tr><th></th><th></th><th>ρ (kg/m³)</th><th>c_p (J/kgK)</th><th>k (W/mK)</th><th>ν (m²/s)</th><th>σ (N/m)</th><th>h_{lv} (J/kg)</th></tr>
<tr><td rowspan="2">Phase properties (R113 at 1bar, T_{sat} = 320.65 K)</td><td>Liquid</td><td>1508.4</td><td>940.3</td><td>0.064</td><td>3.25×10^{-7}</td><td rowspan="2">0.015</td><td rowspan="2">144350</td></tr>
<tr><td>Vapour</td><td>7.4</td><td>691.3</td><td>0.0095</td><td>1.39×10^{-6}</td></tr>
<tr><td rowspan="3">Initial Conditions</td><td colspan="2" rowspan="2">Initial bubble (seed) radius (μm): 50</td><td colspan="3">Wall superheat (K): 13.5</td><td colspan="2" rowspan="2">Domain size (mm): 2.5x4.0</td></tr>
<tr><td colspan="3">Contact angle (°): 11.4 (Series A), 30 (Series B,C and D)</td></tr>
<tr><td colspan="2">Initially developed thermal boundary layer thickness (μm): 352</td><td colspan="3">Simulation Type: Axisymmetric</td><td colspan="2">No. of computational cells: 400000</td></tr>
</table>

Table 5. Fluid properties and initial conditions (Base case for R22 refrigerant, Series B, C and D).

<table>
<tr><th></th><th></th><th>ρ (kg/m³)</th><th>c_p (J/kgK)</th><th>k (W/mK)</th><th>ν (m²/s)</th><th>σ (N/m)</th><th>h_{lv} (J/kg)</th></tr>
<tr><td rowspan="2">Phase properties (R22 at 1bar, T_{sat} = 232.06K</td><td>Liquid</td><td>1410.0</td><td>1089.2</td><td>0.1135</td><td>2.46×10^{-7}</td><td rowspan="2">0.015</td><td rowspan="2">217160</td></tr>
<tr><td>Vapour</td><td>4.65</td><td>605.61</td><td>0.0070</td><td>1.88×10^{-6}</td></tr>
<tr><td rowspan="3">Initial Conditions</td><td colspan="2" rowspan="2">Initial bubble (seed) radius (μm): 50</td><td colspan="2">Wall superheat (K): 13.5</td><td colspan="3" rowspan="2">Domain size (mm): 2.5x4.0</td></tr>
<tr><td colspan="2">Contact angle (°): 30</td></tr>
<tr><td colspan="2">Initially developed thermal boundary layer thickness (μm): 352</td><td colspan="2">Simulation Type: Axisymmetric</td><td colspan="3">No. of computational cells: 400000</td></tr>
</table>

Table 6. Fluid properties and initial conditions (Base case for R134a refrigerant, Series B, C and D).

		ρ (kg/m³)	c_p (J/kgK)	k (W/mK)	ν (m²/s)	σ (N/m)	h_{lv} (J/kg)
Phase properties (R134a at 1bar, T_{sat} = 246.79K)	**Liquid**	1377.5	1280.0	0.104	2.76×10^{-7}	0.015	144350
	Vapour	5.19	793.19	0.0093	1.39×10^{-6}		
Initial Conditions	Initial bubble (seed) radius (μm): 50		Wall superheat (K): 13.5 Contact angle (°): 30		Domain size (mm): 2.5x4.0		
	Initially developed thermal boundary layer thickness (μm): 352		Simulation Type: Axisymmetric		No. of computational cells: 400000		

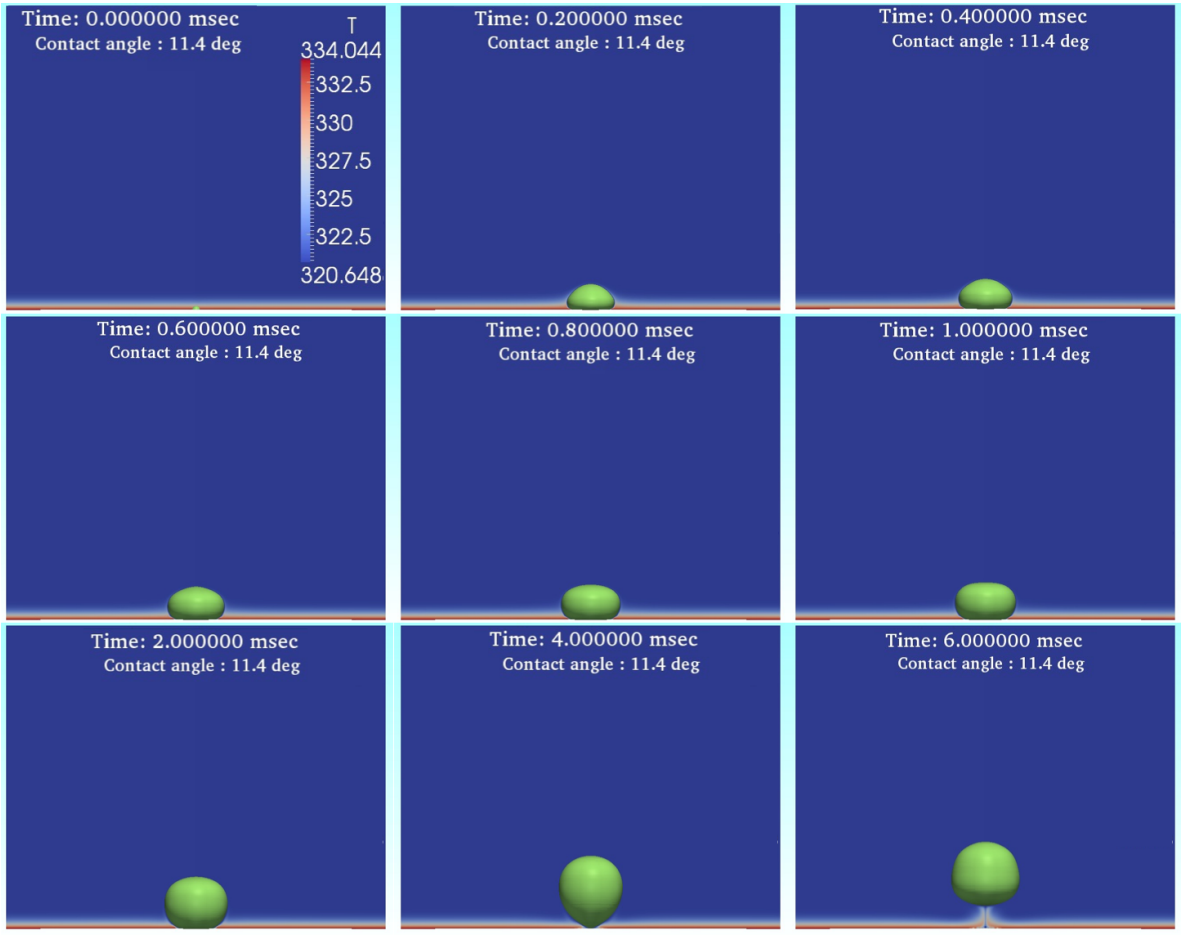

Figure 10. 3D bubble spatial and temporal evolution (base case, R113).

The temporal and spatial evolution of the bubble growth and detachment process for the base case of Table 4, is depicted indicatively in Fig. 10, where the interface position between the vapour and liquid phases (green surface) is illustrated for successive time instances, from the 3D reconstruction of the axisymmetric simulation results.

As it can be observed the initially seeded bubble nucleus (t = 0 ms) grows and finally detaches from the superheated wall. As it was expected, initially, the bubble base diameter increases since the

evaporating meniscus on the bubble foot slides outwards up to a certain point, and finally decreases sliding inwards up to the instance of detachment. After the detachment from the heated wall the bubble rises in the liquid domain due to buoyancy. Furthermore, a characteristic depletion of the thermal boundary layer is observed after the bubble detachment, while the rising bubble curries some heat upwards in its tail. These qualitative observations are in agreement with previous similar investigations (e.g. [58], [81,82]).

4.1 Effect of initial thermal boundary layer – Series A

Since the superheated bulk liquid thermal boundary layer thickness, determines how much heat is stored in the fluid layer in the vicinity of the heated plate, it was deemed appropriate for a parametric study to be conducted, aiming to identify the effect of the Initial Thermal Boundary Layer (ITBL) thickness, on the bubble growth and detachment process. Therefore, in the current sub-section of the present paper, the effect of the ITBL on the bubble detachment characteristics is investigated numerically. For this purpose, the base case of Table 4 is utilised and additional simulations are performed by systematically varying the ITBL that is imposed, as an initial condition, in the vicinity of the heated plate (bottom wall boundary of the computational domain). In more detail, a single-phase transient simulation is first performed and the developed thermal boundary layers are extracted in certain successive time steps. These are then used as the initial condition for the temperature field, in the two-phase numerical simulations that comprise the proposed parametric analysis (Series-A numerical simulations). All the other simulation parameters are kept constant with respect to the base simulation case (Table 4). Details regarding the overall runs conducted are summarised in Table 7.

Table 7. Varied parameter in Series-A of parametric numerical simulations.

Run	Time of ITBL development (Single-phase simulation) [sec]	Thickness of ITBL [μm]
A1	0.01	136
A2	0.02	184
A3	0.03	216
A4	0.06	304
A5	0.07	328
A6 (base case, R113)	0.08	352
A7	0.09	376
A8	0.1	392
A9	0.2	552
A10	0.3	680

As it can be observed a total number of nine additional simulations were performed changing in each case the initial temperature field. The reference/base case in Table 7 corresponds to the validation run of Fig. 9. The prescribed ITBL in each case is illustrated diagrammatically in Fig. 11, where the initial variation of temperature with respect to the vertical distance from the heated plate is plotted for each run of Series A numerical simulations.

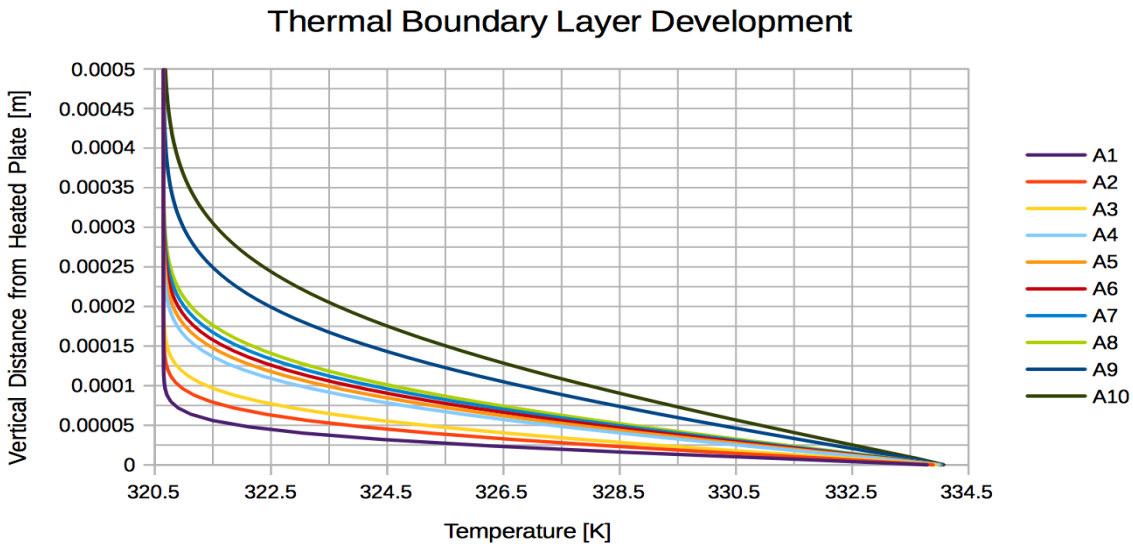

Figure 11. ITBL for each run of Series-A parametric numerical simulations.

The spatial evolution of the generated bubbles for each of the above cases at the time of detachment, is depicted in Fig. 12. As it can be observed, there is a substantial increase in the bubble growth and detachment characteristics with respect to the corresponding increase in the thickness of the ITBL. The thicker the ITBL, the bigger the bubble diameter at detachment. These findings are in direct qualitative agreement with previous similar investigations (e.g. [83]).

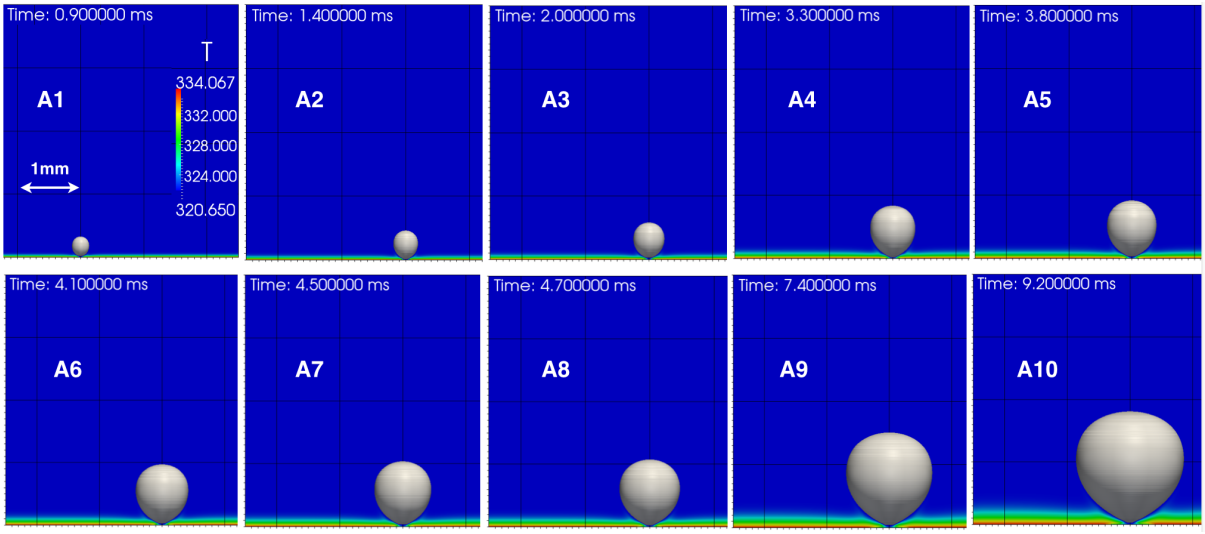

Figure 12. Spatial evolution of generated bubble at the time of detachment for each case of Series–A.

The bubble detachment time with respect to the ITBL thickness is plotted in Fig. 13a, while the equivalent bubble detachment diameter with respect to the ITBL thickness is plotted in Fig. 13b. It should be mentioned here that the diameter of a sphere, having the same volume as the corresponding in each case bubble at the time of detachment from the heated plate, is taken as the equivalent bubble detachment diameter.

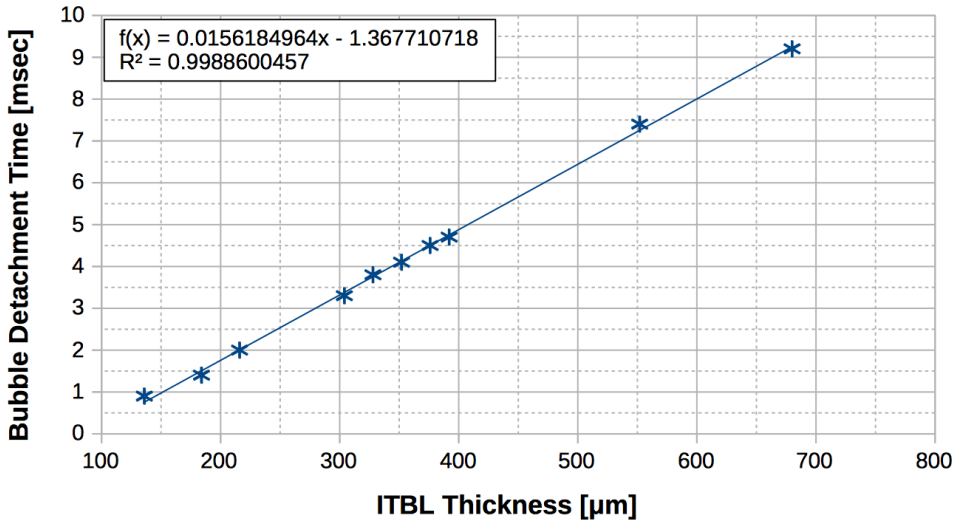

(a)

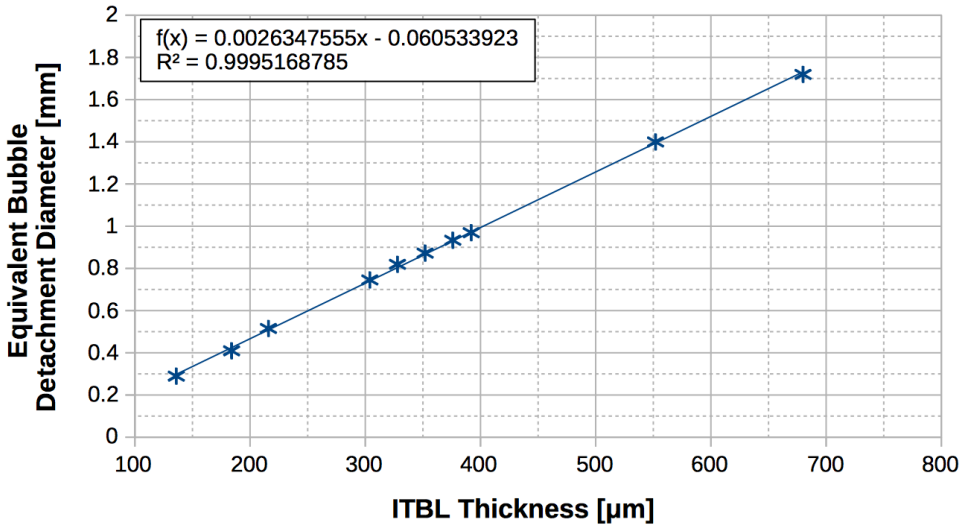

(b)

Fig. 13. Effect of ITBL thickness on: (a) the bubble detachment time; (b) the equivalent bubble detachment diameter.

As it can be observed the increase of the ITBL causes a linear increase in both the bubble detachment time as well as the equivalent bubble detachment diameter. It is characteristic that an increase of the ITBL by a factor of five causes a corresponding increase in the bubble detachment time and the equivalent bubble detachment diameter by a factor of nine and six, respectively. From all the above, it is evident that the ITBL is a very influential and important parameter in the bubble growth and detachment process.

Therefore, it is strongly suggested that the bulk liquid thermal boundary layer thickness should be measured and reported in future experimental studies, since it comprises a required input for the successful numerical simulation of nucleate boiling processes.

4.2 Effect of surface wettability – Series B

Past studies have identified surface wettability as one of the most important factors affecting bubble nucleation, growth and detachment (e.g. [62], [84–86]) provide a good summary of the current understanding. The effect of surface wettability on bubble growth can be incorporated in a numerical model by the imposed contact angle between the vapour/liquid interface and the heated solid surface (triple-line). In the current section of the present paper the effect of wettability on the bubble detachment characteristics, is investigated numerically. For this purpose, the base cases of Tables 4,

600 5 and 6 are utilised and additional simulations are performed by systematically varying the value of
601 the triple-line (solid-liquid-vapour) contact angle at the bottom wall boundary of the computational
602 domain. All the other simulation parameters are kept constant with respect to the base simulation
603 cases (Tables 4, 5 and 6). Details regarding the overall runs are summarised in Table 8.

604 **Table 8.** Varied parameter in Series-B of parametric numerical simulations.

Run	Contact Angle (°)	Working Fluid	Run	Contact Angle (°)	Working Fluid	Run	Contact Angle (°)	Working Fluid
B1 (Base Case R113)	11.4	R113	**B16**	15	R22	**B31**	15	R134a
B2	15	R113	**B17**	20	R22	**B32**	20	R134a
B3	20	R113	**B18**	25	R22	**B33**	25	R134a
B4	25	R113	**B19 (base case, R22)**	30	R22	**B34 (base case, R134a)**	30	R134a
B5	30	R113	**B20**	35	R22	**B35**	35	R134a
B6	35	R113	**B21**	40	R22	**B36**	40	R134a
B7	40	R113	**B22**	45	R22	**B37**	45	R134a
B8	45	R113	**B23**	50	R22	**B38**	50	R134a
B9	50	R113	**B24**	55	R22	**B39**	55	R134a
B10	55	R113	**B25**	60	R22	**B40**	60	R134a
B11	60	R113	**B26**	65	R22	**B41**	65	R134a
B12	65	R113	**B27**	70	R22	**B42**	70	R134a
B13	70	R113	**B28**	75	R22	**B43**	75	R134a
B14	75	R113	**B29**	80	R22	**B44**	80	R134a
B15	80	R113	**B30**	85	R22	**B45**	85	R134a

605
606 As it can be seen, a total of 45 simulations are performed, varying the imposed contact angle at
607 the bottom wall boundary from 11.4° up to 80° for the case of R113 runs (B1 to B15) and from 15° to
608 85° for the cases of R22 (B16 to B30) and R134a (B31 to B45). The spatial evolution of the generated
609 bubbles for each of the above cases, at the time of detachment, is depicted in Figures 14, 15, and 16,
610 for the R113, R22 and R134a cases, respectively.
611

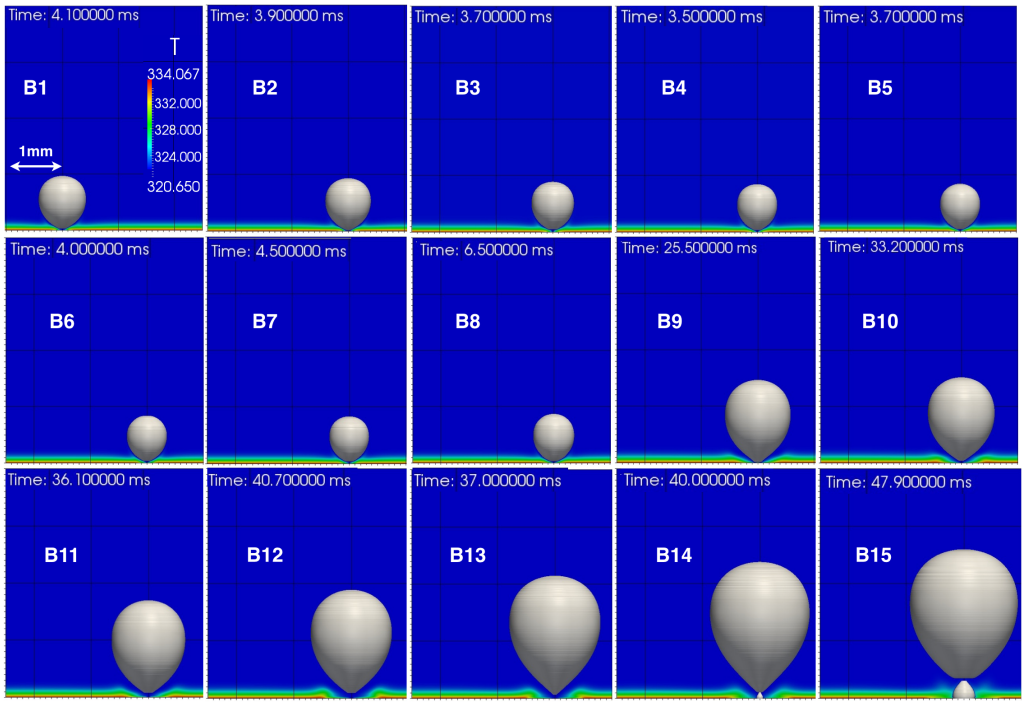

Figure 14. Spatial evolution of generated bubble at the time of detachment for each R113 case of Series –B parametric numerical simulations.

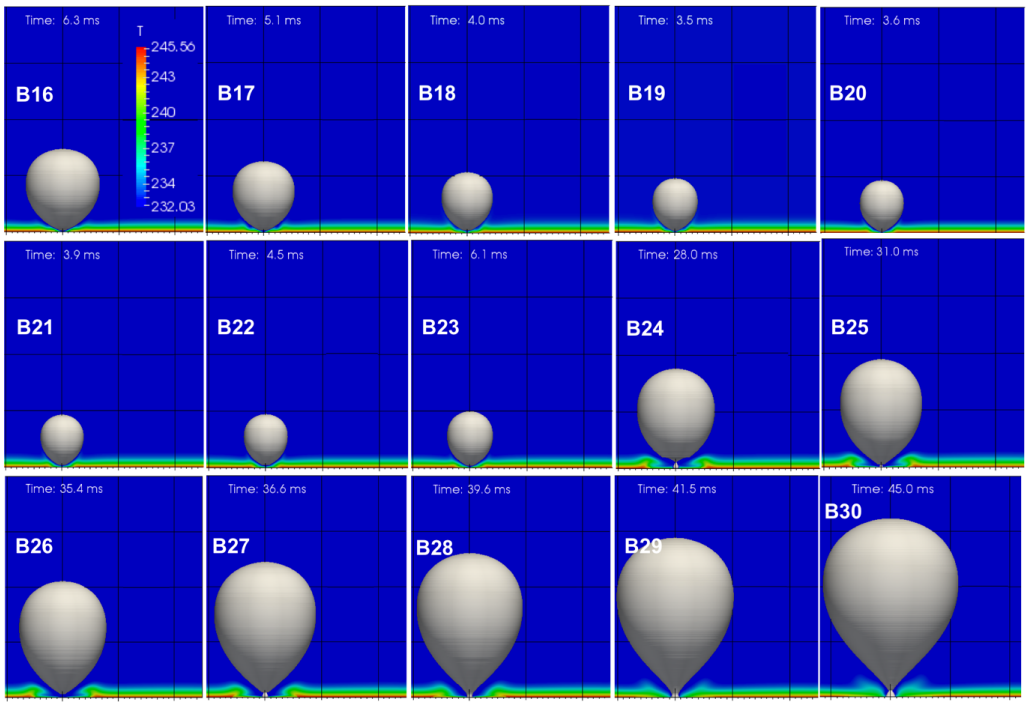

Figure 15. Spatial evolution of generated bubble at the time of detachment for each case R22 of Series –B parametric numerical simulations.

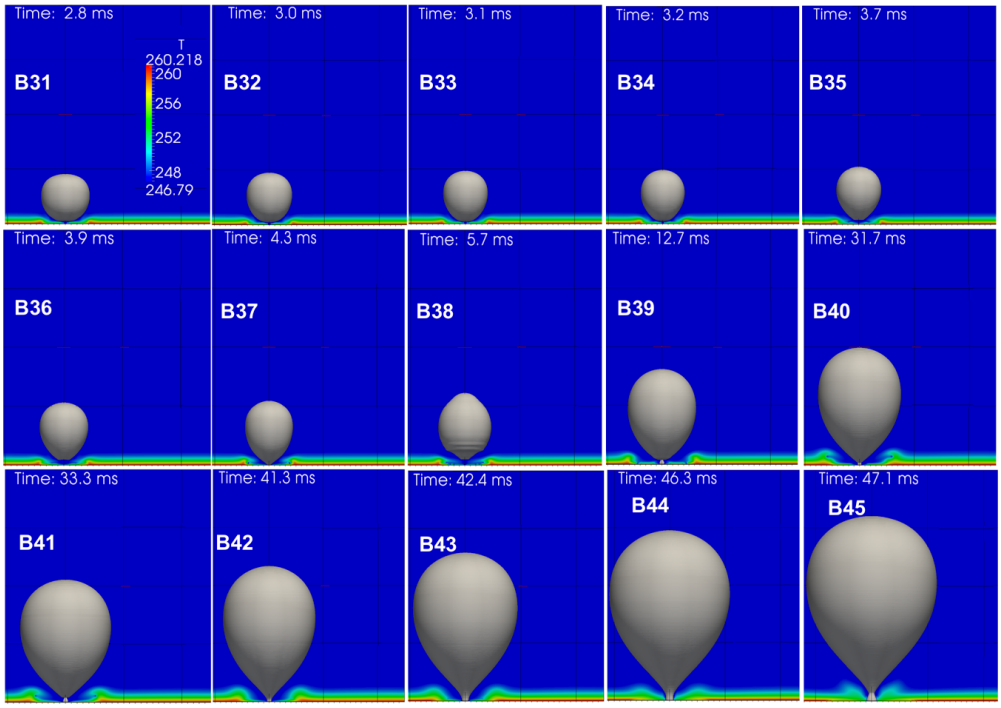

Fig. 16. Spatial evolution of generated bubble at the time of detachment for each R134a case of Series –B parametric numerical simulations.

As it can be observed from Fig. 14, for the R113 runs, initially the successive increase of the imposed contact angle from 11.4° (case B1) up to 45° (case B8) has a relatively minimal effect in the bubble detachment characteristics. On the other hand, for equilibrium contact angles greater than 45° (cases B9 to B15), the effect of the contact angle in both the bubble detachment volume and the bubble detachment time, appears to be quite more significant. In more detail, the bubble detachment volume slightly decreases (cases B2 and B3) and then remains almost constant (cases B4-B8). However, a slightly different effect can be observed in the predicted bubble detachment times. The bubble detachment time initially shows a small decrease (cases B2 to B4), and then it successively starts to show a small increase again (cases B5 to B8). When the imposed contact angle successively increases above 45° (cases B9-B15), it causes a subsequent increase in the bubble detachment volume. Approximately the same trend can be observed also in the bubble detachment time.

However, it is characteristic that while the bubble detachment time continuously increases with the corresponding increase in the contact angle (cases B9-B12) at a certain point (cases B13 and B14) remains almost constant and then continues to increase (case B15).

Another interesting observation is the fact that for contact angles greater than 70° (cases B14 and B15), the bubble departs from the heated surface leaving behind a small residual bubble nucleus on the surface.

For the R113 runs (Fig. 15), the successive increase of the imposed contact angle from 15° up to 45° (cases B16 to B22) has a relatively small effect in the bubble detachment characteristics. However, as in the case of R113 runs, there is a significantly higher effect of the contact angle increase, in both the bubble detachment time and volume, for contact angles greater than 45°. In more detail, there is a small successive degrease in the bubble detachment volume as the contact angle increases from 15° to 30° (cases B16-B19) and then it remains constant from 35° to 45° (cases B20-B22). For angles greater than 45°, the successive increase of the contact angle causes a significant increase in the bubble detachment volume (B23-B30). A similar behaviour can also be observed for the bubble detachment time.

Finally, for the R134a runs (Fig. 16), an almost negligible effect of the contact angle increase on both the bubble detachment time and bubble detachment volume can be observed for contact angles lower than 45°, while a significant increase in the bubble detachment characteristics is evident with the corresponding increase of the imposed contact angle for values greater than 45°.

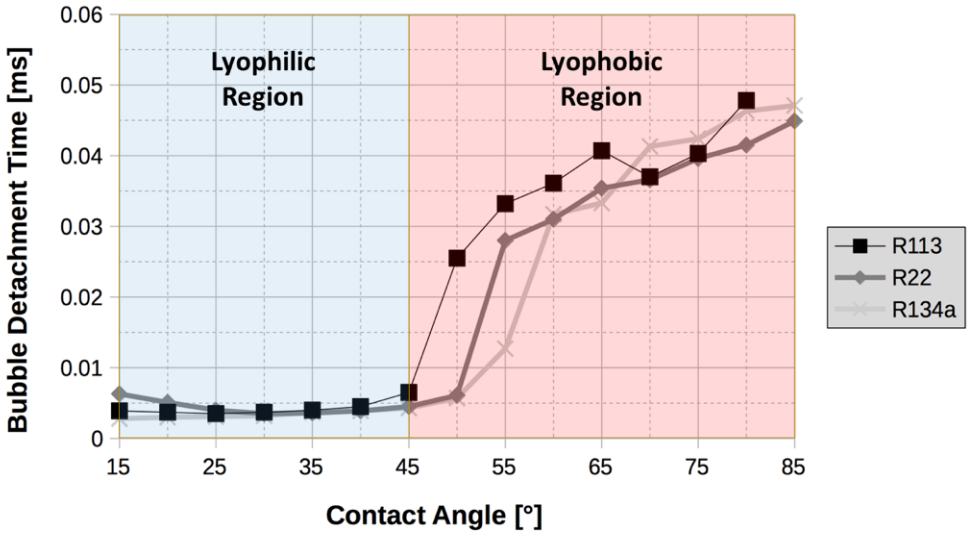

(a)

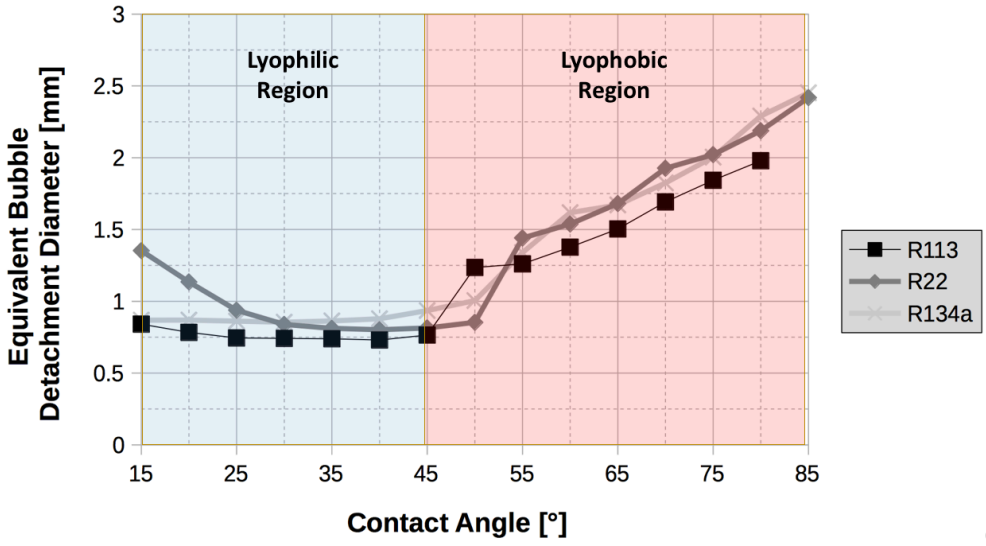

(b)

Figure 17. Effect of contact angle on: (a) the bubble detachment time; (b) the equivalent bubble detachment diameter.

As it can also be confirmed by the diagrams of Fig. 17, the bubble detachment characteristics seem to be significantly affected by the imposed contact angle, i.e. the wettability of the heated plate, for values higher than 45° showing an irregular increase. However, the proposed effect is minimal for contact angles lower than this limiting value of 45°. It is important to note that in total, for each of the considered working fluids, increasing the contact angle by an approximate factor of 8 causes a significant increase in the bubble detachment time by a factor of 10, while the equivalent bubble detachment diameter increases by a smaller but still significant factor of approximately 3.

Therefore, it is evident that two distinct behavioral regions can be identified in the diagrams of Fig. 17, that are common for all the three examined working fluids. A "lyophilic" region ($\theta \leq 45^{o}$) without significant changes in the bubble detachment characteristics and a "lyophobic" region ($\theta > 45^{o}$) were both the bubble detachment time and the equivalent bubble detachment diameter are highly affected by the wettability of the heated plate. According to the authors' best knowledge there are not, at the moment, any experimental demonstrations of this phenomenon.

Cases with even higher contact angles where also tested, for the case of R113 (up to a value of 160°). For this purpose, a bigger computational domain was constructed (5 mm x 8 mm) keeping the same computational mesh characteristics as the ones described in Section 3.2.2. Some indicative results are depicted in Fig. 18, where the spatial evolution of the generated bubbles after

approximately 50 ms from the nucleation time is depicted, for four different cases with corresponding contact angle values of 90°, 115°, 130° and 140°, respectively.

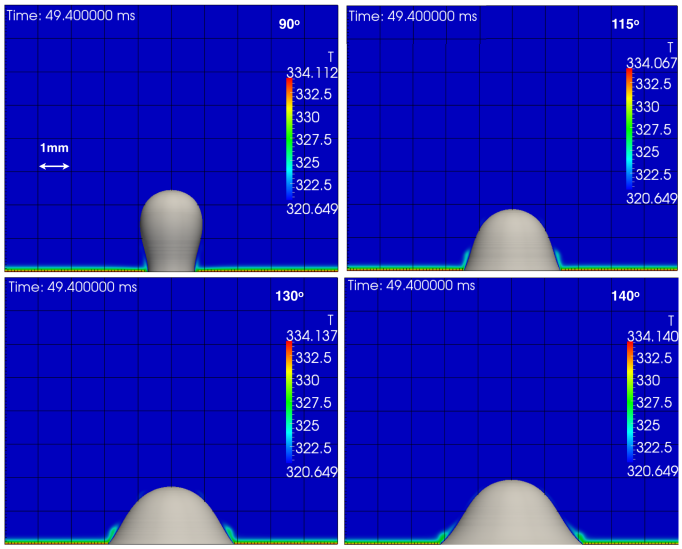

Figure 18. Evolution of a R113 bubble, at t=49.40 ms, for equilibrium contact angles higher than 80°.

As it can be observed, as the contact angle increases beyond the value of 80°, the bubble detachment time subsequently increases significantly and especially after a contact angle of 100°, the bubble continuously grows and its initial meniscus continuously slides outwards tending to form a vapour film. This observation is in direct qualitative agreement with previous investigations of pool boiling of water in hydrophilic, hydrophobic and super-hydrophobic surfaces (e.g. [87,88]). An example on the generated bubble before detachment for a hydrophilic (contact angle of 30°) and a hydrophobic (contact angle of 150°) surface, from the work of Malavasi et al. [88], is given in the experimental snapshots of Fig. 19.

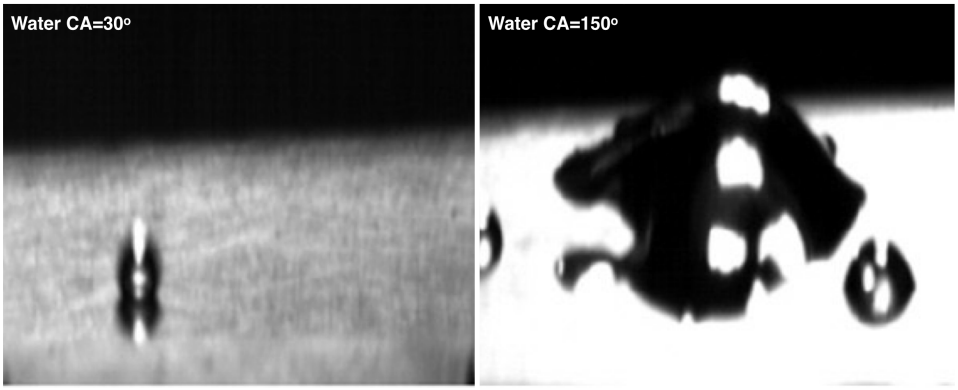

Figure 19. Experimental images of pool boiling of water on hydrophilic and hydrophobic surfaces [88].

As it can be seen, in the case of the hydrophilic surface the shape of the bubble before its detachment is more close to case B4 of the present investigation (Fig. 14) while the case of the hydrophobic surface is in close qualitative agreement with the case of 140° of Fig. 18.

All the above findings indicate that the wettability of the heated surface in nucleate boiling is another quite important factor that significantly affects the bubble growth and detachment characteristics.

697 *4.3 Effect of wall superheat – Series C*

698 In the current sub-section of the present paper the effect of wall superheat on the bubble
699 detachment characteristics, is investigated numerically. For this purpose, the base cases of Table 4, 5
700 and 6 are utilised and additional simulations are performed by systematically varying the value of
701 the heated plate superheat (bottom wall boundary of the computational domain). All the other
702 simulation parameters are kept constant with respect to the base simulation cases. Details regarding
703 the overall runs conducted are summarised in Table 9.
704

705 **Table 9.** Varied parameter in Series-C of parametric numerical simulations.

Run	Wall Superheat (K)	Working Fluid	Run	Wall Superheat (K)	Working Fluid
C1	5.5	R113	**C16**	17.5	R22
C2	10.5	R113	**C17**	18.5	R22
C3 (base case, R113)	13.5	R113	**C18**	19.5	R22
C4	14.5	R113	**C19**	2.5	R134a
C5	15.5	R113	**C20**	5.5	R134a
C6	16.5	R113	**C21**	10.5	R134a
C7	17.5	R113	**C22 (base case R134a)**	13.5	R134a
C8	18.5	R113	**C23**	14.5	R134a
C9	19.5	R113	**C24**	16.5	R134a
C10	2.5	R22	**C25**	17.5	R134a
C11	5.5	R22	**C26**	18.5	R134a
C12	10.5	R22	**C27**	19.5	R134a
C13 (base case R22)	13.5	R22			
C14	14.5	R22			
C15	16.5	R22			

706
707 As it can be seen, a total of 27 simulations are performed, varying the bottom wall superheat
708 from 5.5 K up to 19.5 K for the R113 runs and from 2.5 K up to 19.5 K for the R22 and R134a runs,
709 respectively. It should be mentioned here that as for the validation case (C3) a single-phase transient
710 numerical simulation is initially performed in each of the above cases and the developed ITBL at 0.08s
711 is used as the initial condition for the temperature field in the two-phase simulations. This is done in

order to start in each case with approximately the same thickness of the ITBL but with a different superheat. The spatial evolution of the generated bubbles for each of the above cases, at the time of detachment, is depicted in Fig. 20, 21 and 22 for the R113, R22 and R134a runs, respectively.

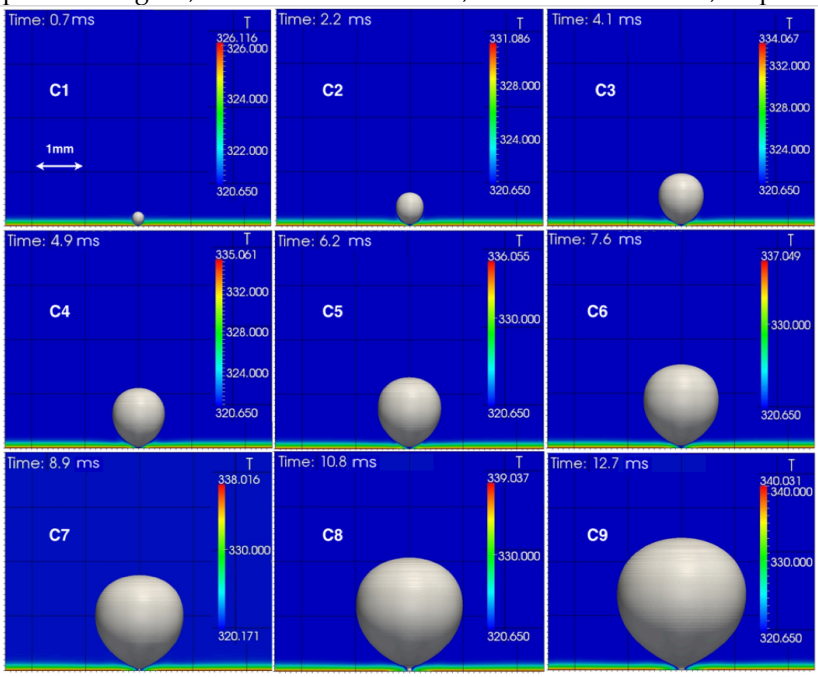

Figure 20. Spatial evolution of generated bubble at the time of detachment for each R113 case of Series –C parametric numerical simulations.

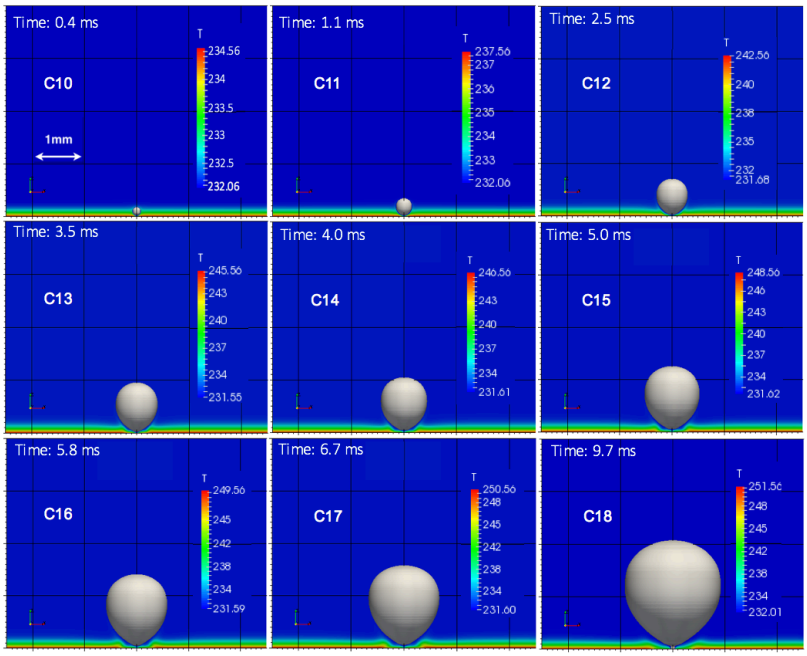

Figure 21. Spatial evolution of generated bubble at the time of detachment for each R22 case of Series –C parametric numerical simulations.

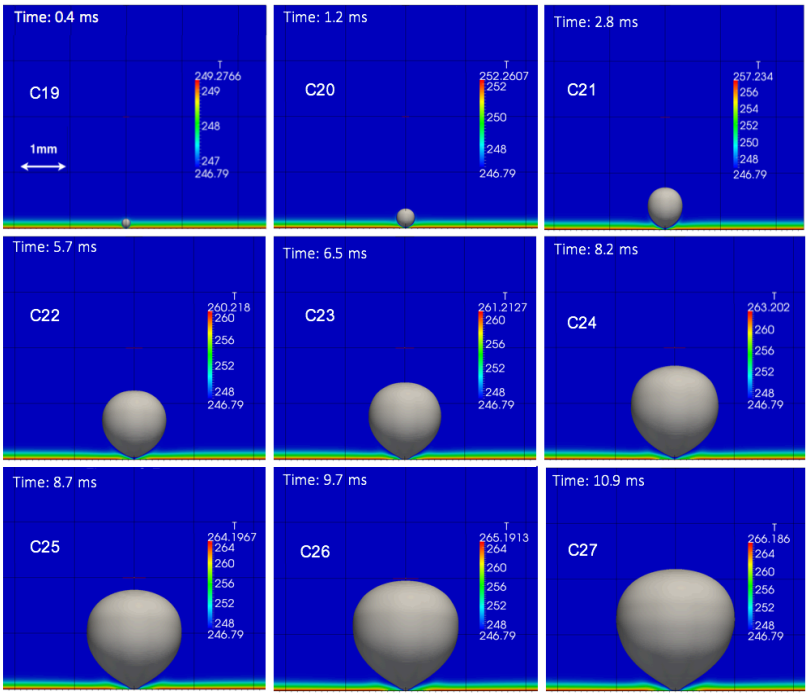

Figure 22. Spatial evolution of generated bubble at the time of detachment for each R134a case of Series –C parametric numerical simulations.

As it can be observed both the bubble detachment time as well as the bubble detachment volume are highly sensitive to the wall superheat. In more detail, a successive increase in the bottom wall superheat causes a quite considerable subsequent increase in the bubble detachment characteristics. But in order to quantify the exact influence of the wall superheat on the bubble detachment characteristics, the diagrams of Fig. 23 are plotted. In more detail, the bubble detachment time with respect to the applied wall superheat is plotted in Fig. 23a, while the equivalent bubble detachment diameter is plotted in Fig. 23b.

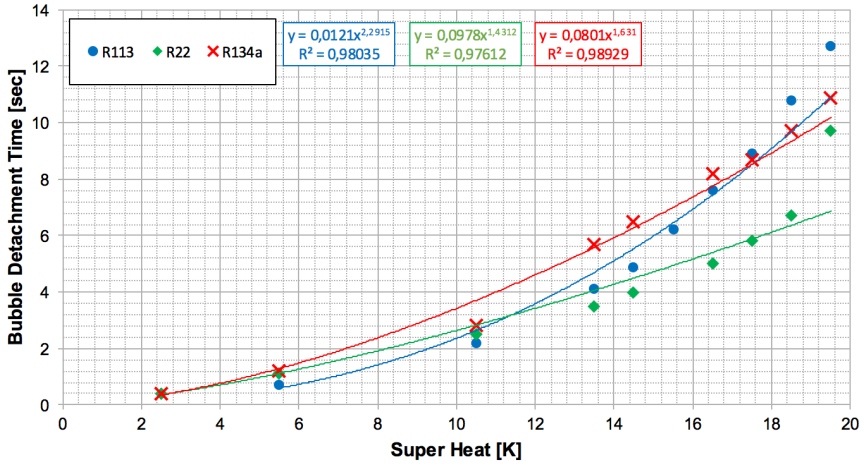

(a)

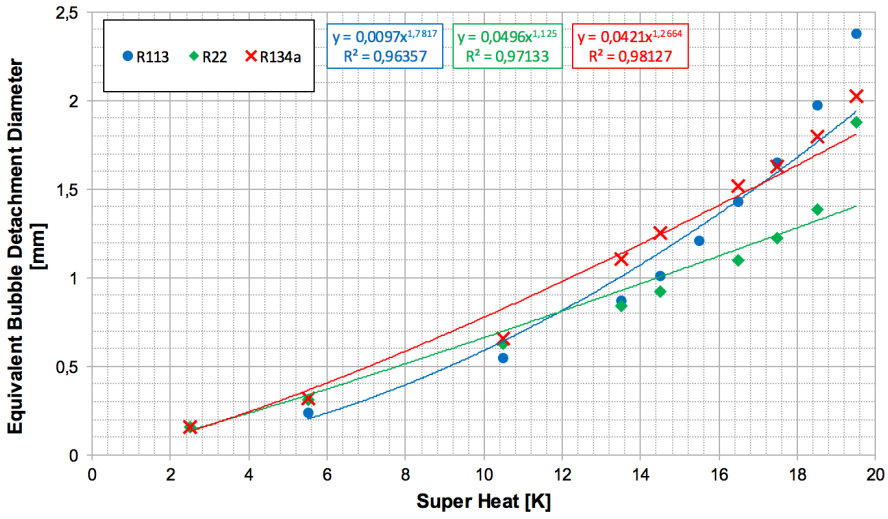

(b)

Figure 23. Effect of wall superheat on (a) the bubble detachment time and (b) the equivalent bubble detachment diameter.

As it can be observed the increase of the applied wall superheat causes a subsequent increase in both the bubble detachment time as well as the equivalent bubble detachment diameter, following a power law, for all three of the examined working fluids. It is characteristic that an increase in the applied superheat by a factor of just 3.5, causes a corresponding increase in the bubble detachment time and the equivalent bubble detachment diameter by an approximate factor of 18 and 10 for R113 and 9 and 6 for R22 and R134a. All these findings and observations are in direct qualitative agreement with previous similar investigations (e.g. [89]).

As expected, the value of the heated wall superheat is a very important parameter in the bubble growth and detachment process. Even a temperature variation of a few degrees can significantly alter the bubble detachment characteristics. Therefore, it can be concluded that the accurate measurement of the temperature values in the vicinity of the generated bubbles is quite crucial for the numerical reproduction of experimental results on nucleate boiling.

4.4 Effect of Gravity Level – Series D

In the current sub-section of the present paper the effect of gravity level on the bubble detachment characteristics, is investigated numerically. For this purpose, the base cases of Table 4, 5 and 6 are utilised and additional simulations are performed by systematically varying the value of the gravitational acceleration. Five different gravity levels that correspond to the gravitational acceleration values of all the major planets in the Earth's solar system are utilised for the proposed parametric analysis. It must be mentioned that the proposed analysis is again performed for the same working fluids (R113, R22 and R134a) but not only for atmospheric pressure conditions (1 bar) but also for 5 bar ambient pressure conditions. Tables 4, 5 and 6 indicate the utilised fluid properties for 1 bar ambient pressure. The corresponding properties and the initial conditions for the base simulation cases in the case of 5 bar ambient pressure, are summarised in Tables 10, 11 and 12, accordingly. Details regarding the varying parameter and the overall runs conducted for Series D of parametric numerical simulations, are summarised in Table 13.

766 **Table 10.** Fluid properties and initial conditions (Base case for R113 refrigerant at 5 bar).

		ρ (kg/m³)	c_p (J/kgK)	k (W/mK)	ν (m²/s)	σ (N/m)	h_{lv} (J/kg)
Phase properties (R113 at 5bar) T_{sat} = 379.02 K	**Liquid**	1351.4	1014.9	0.053	1.94×10^{-3}	0.0086	122950
	Vapour	34.1	790.8	0.012	3.56×10^{-3}		
Initial Conditions	Initial bubble (seed) radius (μm): 50		Wall superheat (K): 13.5			Domain size (mm): 2.5x4.0	
			Contact angle (°): 30				
	Initially developed thermal boundary layer thickness (μm): 352		Simulation Type: Axisymmetric			No. of computational cells: 400000	

767

768 **Table 11.** Fluid properties and initial conditions (Base case for R22 refrigerant, at 5 bar).

		ρ (kg/m³)	c_p (J/kgK)	k (W/mK)	ν (m²/s)	σ (N/m)	h_{lv} (J/kg)
Phase properties (R22 at 5bar) T_{sat} = 273.27 K	**Liquid**	1281.1	1169.6	0.094687	1.68×10^{-3}	0.01168	144350
	Vapour	21.312	739.50	0.009416	5.33×10^{-3}		
Initial Conditions	Initial bubble (seed) radius (μm): 50		Wall superheat (K): 13.5			Domain size (mm): 2.5x4.0	
			Contact angle (°): 30				
	Initially developed thermal boundary layer thickness (μm): 352		Simulation Type: Axisymmetric			No. of computational cells: 400000	

769

770 **Table 12**. Fluid properties and initial conditions (Base case for R134a refrigerant, at 5 bar).

		ρ (kg/m³)	c_p (J/kgK)	k (W/mK)	ν (m²/s)	σ (N/m)	h_{lv} (J/kg)
Phase properties (R134a at 1bar) T_{sat} = 246.79 K	**Liquid**	1240.8	1389.4	0.085126	1.76×10^{-3}	0.00934	185970
	Vapour	24.317	976.12	0.012930	4.70×10^{-3}		
Initial Conditions	Initial bubble (seed) radius (μm): 50		Wall superheat (K): 13.5			Domain size (mm): 2.5x4.0	
			Contact angle (°): 30				
	Initially developed thermal boundary layer thickness (μm): 352		Simulation Type: Axisymmetric			No. of computational cells: 400000	

771

772

773 **Table 13.** Varied parameter in Series-D of parametric numerical simulations.

Run	Gravitational Acceleration (m/s²)	Working Fluid	Run	Gravitational Acceleration (m/s²)	Working Fluid
D1	0.58 (Pluto)	R113	**D16**	0.58	R113
D2	3.71 (Mars/Mercury)	R113	**D17**	3.71	R113
D3	8.83 (Venus/Saturn/Uranus)	R113	**D18**	8.83	R113
D4 (base case, R113, P=1bar)	***9.81 (Earth)***	***R113***	***D19 (base case, R113, P=5bar)***	***9.81***	***R113***
D5	10.99 (Neptune)	R113	**D20**	10.99	R113
D6	0.58	R22	**D21**	0.58	R22
D7	3.71	R22	**D22**	3.71	R22
D8	8.83	R22	**D23**	8.83	R22
D9 (base case, R22, P=1bar)	***9.81***	R22	***D24 (base case, R22, P=5bar)***	***9.81***	***R22***
D10	10.99	R22	**D25**	10.99	R22
D11	0.58	R134a	**D26**	0.58	R134a
D12	3.71	R134a	**D27**	3.71	R134a
D13	8.83	R134a	**D28**	8.83	R134a
D14 (base case, R134a, P=1bar)	***9.81***	***R134a***	***D29 (base case, R134a, P=5bar)***	***9.81***	***R134a***
D15	10.99	R134a	**D30**	10.99	R134a

774

775 As it can be seen, a total of 30 simulations are performed. Four additional simulations for each
776 of the considered working fluids (R113, R22 and R134a) are performed initially, changing the value
777 of the gravitational acceleration from 9.81 m/s2 in the base cases (D4, D9 and D14, Earth), to 0.58 m/s2
778 (D1, D6 and D11, Pluto), 3.71 m/s2 (D2, D7 and D12, Mars/Mercury), 8.83 m/s2 (D3, D8 and D13,
779 Venus/Saturn/Uranus) and 10.99 m/s2 (D5, D10 and D15, Neptune). Then these simulations are all
780 repeated (D16-D20 for R113, D20-D25 for R22 and D25-D30 for R134a) changing the ambient pressure

781 from 1 to 5 bar, and hence the properties of the liquid and vapour phases (as summarised in Tables
782 10, 11 and 12). The spatial evolution of the generated bubbles for each of the above cases, at the time
783 of detachment, is depicted in Fig. 24 and 25, for the 1 bar ambient pressure cases (D1-D15) and the 5
784 bar ambient pressure cases (D16-D30), respectively.
785

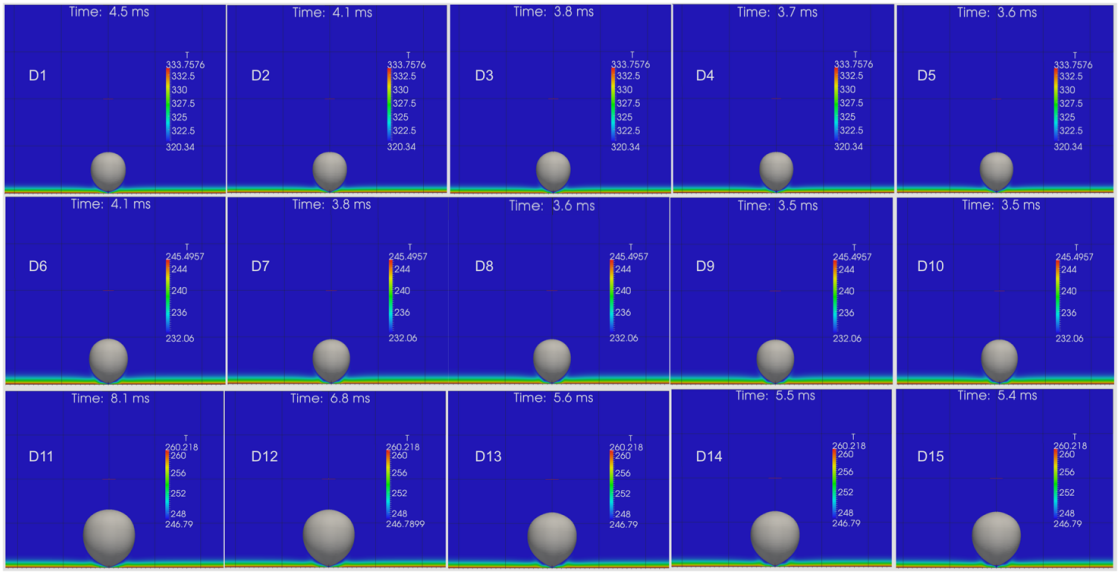

786

787 **Figure 24.** Spatial evolution of generated bubble at the time of detachment for each case of Series –D
788 parametric numerical simulations, with 1 bar ambient pressure condition.

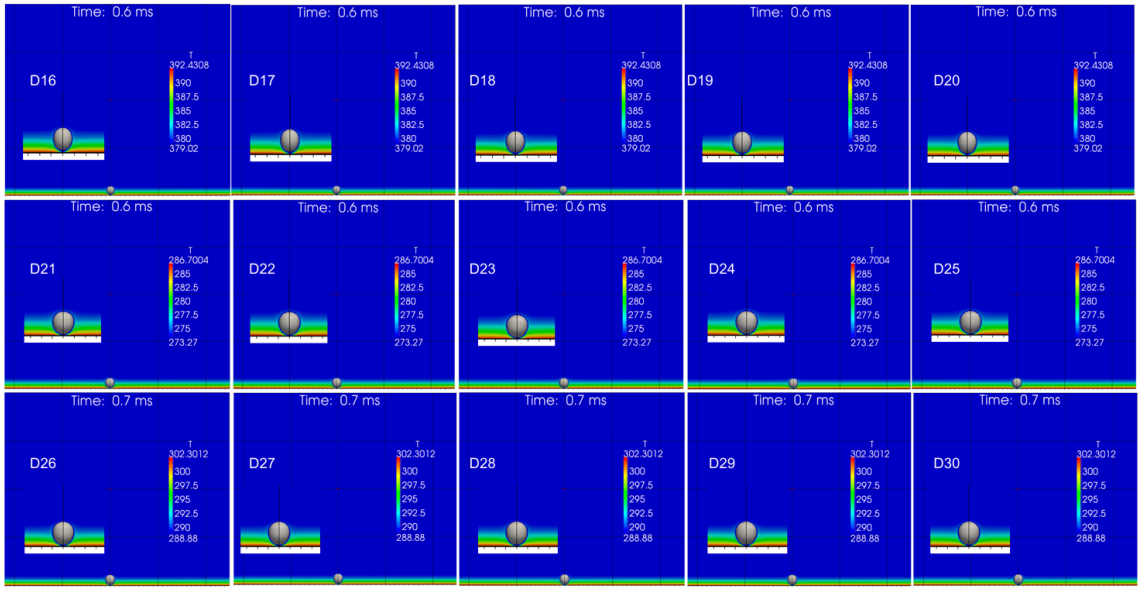

789

790 **Figure 25.** Spatial evolution of generated bubble at the time of detachment for each case of Series –D
791 parametric numerical simulations, with 5 bar ambient pressure condition.

792 As it can be observed from Figure 24, for the cases of 1 bar ambient pressure, both the bubble
793 detachment diameter as well as the bubble detachment time decrease with the corresponding
794 increase of the gravity level. This observation can be explained by the corresponding increase of the
795 acting buoyancy force on the generated in each case bubble. In more details the higher the
796 gravitational acceleration, the higher the acting buoyancy force and therefore the lower the bubble
797 detachment characteristics.
798 However, it is important to notice that for the cases of 5 bar ambient pressure (Figure 25), both
799 the bubble detachment time as well as the bubble detachment volume seem to be unaffected by the

increase in the applied gravitational acceleration, for all three of the examined working fluids. This can be seen in more detail in the diagrams of Fig. 26 and 27, where the bubble detachment time (Figures 26a and 27a) as well as the equivalent bubble detachment diameter (Figures 26b and 27b) are plotted with respect to the applied gravitational acceleration for the cases of 1 bar (Figure 26) and 5 bar (Figure 27) ambient pressure, respectively.

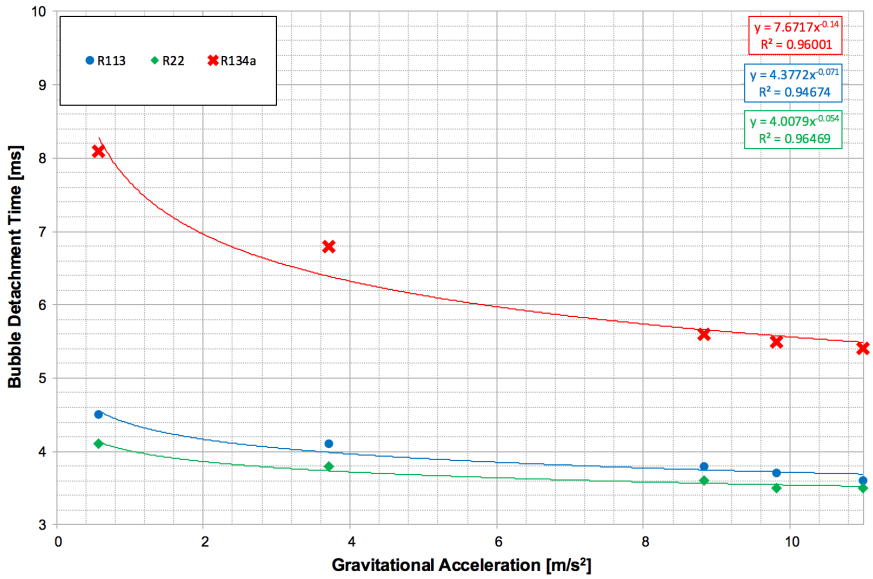

(a)

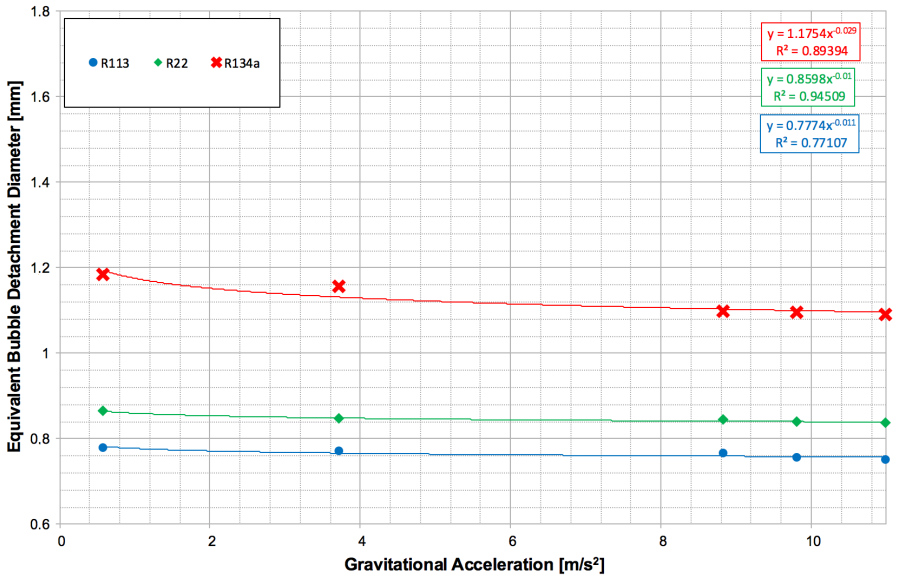

(b)

Figure 26. Effect of gravity level on: (a) the bubble detachment time; (b) the equivalent bubble detachment diameter (cases D1-D15, with 1 bar ambient pressure condition).

As it can be observed from Figure 26a, for all three of the examined working fluids, the bubble detachment time decreases with the corresponding increase on the applied gravitational acceleration, following a power law. It is characteristic to notice that the rate of decrease is initially higher for the case of R134a, while the other two considered refrigerants (R113 and R22) show a similar rate of decrease in the bubble detachment time with respect to the corresponding increase in the gravity level. A similar overall behaviour can be observed for the equivalent bubble detachment diameter (Figure 26b). It is characteristic that a total variation of the gravitational acceleration by a factor of

almost 19 causes a relatively low variation in the bubble detachment time and equivalent bubble detachment diameters by a factor of 1.27 and 1.02, respectively.

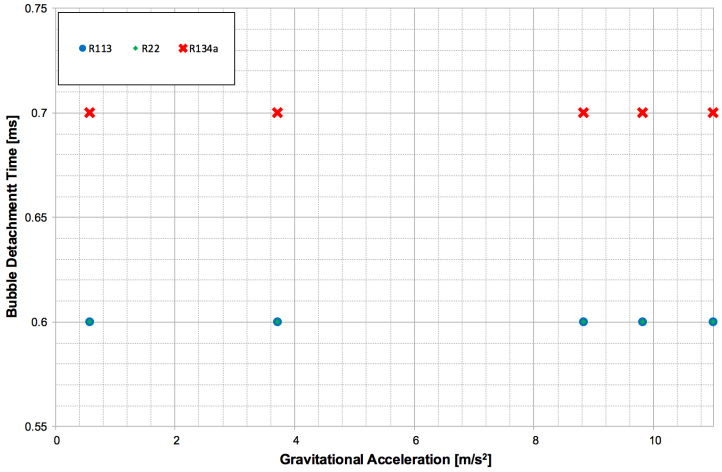

(a)

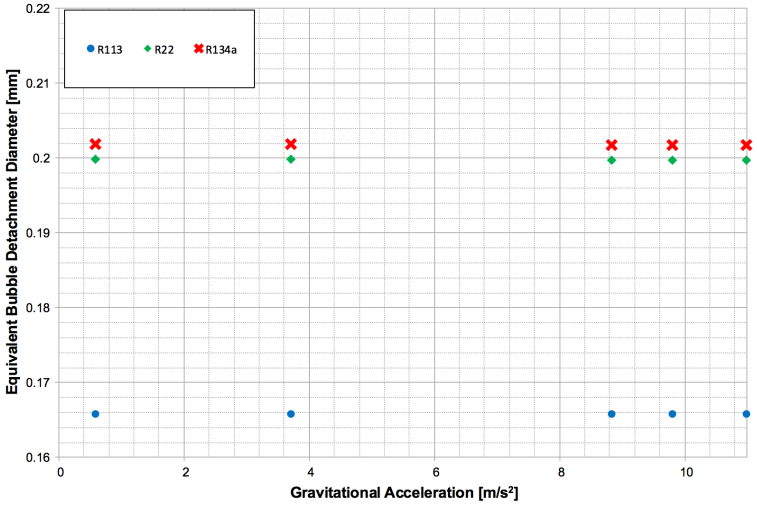

(b)

Figure 27. Effect of gravity level on: (a) the bubble detachment time; (b) the equivalent bubble detachment diameter (cases D16-D30, with 5 bar ambient pressure condition).

Examining the diagrams of Figure 27, it can be concluded that increasing the ambient pressure level of the system from 1 bar to 5 bar it seems that the previously identified effects of gravity level (Figure 26) are diminishing. Furthermore, it is evident that in general, increasing the pressure level the bubble detachment characteristics decrease significantly.

Finally, in order to compare the relative importance of the overall examined controlling parameters in the bubble detachment characteristics, Table 14 summarizes the variation factors in the bubble detachment time and equivalent bubble detachment diameter with respect to the corresponding variation factors for each of the examined controlling parameters, for the cases of R113 refrigerant that is common to all of the conducted series of parametric numerical experiments.

Table 14. Comparison of relative importance of the effect of the examined controlling parameters in the bubble detachment characteristics (R113). Resulting change factors in the bubble detachment characteristics with respect to the maximum variation factors in the examined controlling parameters.

	T_{det} variation factor	D_{eq} variation factor
Initial Thermal Boundary Layer variation factor: 5	9	6
Contact Angle variation factor: 8	10	3
Heated Plate Superheat variation factor: *3.5*	18	10
Gravitational acceleration variation factor: 18.9	1.27	1.02

As it can be observed, according to the overall parametric numerical simulations, the heated plate superheat seems to be the most influential parameter in the bubble detachment characteristics. Quite important is also the influence of the ITBL and the surface wettability. Finally, the gravitational acceleration seems to have a minor influence both in the bubble detachment time (T_{det}) as well as in the equivalent bubble detachment diameter (D_{eq}).

5. Conclusions

In the present paper, an enhanced, algebraic VOF (Volume of Fluid) based interface capturing approach that has been already implemented in the CFD ToolBox of OpenFOAM® (v.2.2.1) [67], is further coupled with heat transfer and phase change for the conduction of axisymmetric numerical experiments on pool boiling. The main goal was the identification of the exact quantitative effect of fundamental parameters on the bubble growth dynamics, focusing on the detachment characteristics of isolated vapour bubbles (from inception to departure), emanating from heated plates submerged in saturated liquid pools. Prior to the main applications the development of the proposed enhanced VOF model is quantitatively validated against an existing analytical solution and literature available experimental data, showing an excellent degree of convergence. The optimised and validated version of the numerical model is then applied for the conduction of four wide series of parametric numerical simulations identifying and quantifying the effects of the Initial Thermal Boundary Layer (ITBL) thickness, the surface wettability (triple-line contact angle), the heated plate superheat and the gravity level, on the bubble detachment characteristics. From the overall analysis and discussion of the results the following important conclusions can be withdrawn:

- Among the examined fundamental controlling parameters, it is shown that the heated plate Superheat constitutes the most influential parameter, followed by the ITBL and the heated surface wettability (contact angle). For the examined flow conditions, the less influential parameter seems to be the applied gravitational acceleration.
- Both the bubble detachment diameter as well as the bubble detachment time, linearly increase with respect to the corresponding increase of the ITBL thickness, for the case of the R113 refrigerant. Therefore, it can be concluded that the bulk liquid thermal boundary layer thickness should always be measured and reported in future experimental studies, since it comprises a required input for the successful numerical simulation of nucleate boiling processes.
- For all three of the considered working fluids (R113, R22 and R134a), the bubble detachment characteristics seem to be significantly affected by the imposed contact angle (wettability of the heated plate) for values higher than a critical contact angle, which is for the considered refrigerant equal to 45°. However, the proposed effect is minimal for contact angles lower that this limiting value of 45°. This finding leads to the identification of two distinct regions a "Lyophilic" region for contact angles lower than 45° and a "Lyophobic" region for contact angles higher that 45°.
- It is also found that the increase of the applied wall superheat causes a power law increase in

878 both the bubble detachment time as well as the equivalent bubble detachment diameter, for all
879 three of the examined working fluids (R113, R22 and R134a). Temperature variations of even a
880 few degrees, can significantly alter the bubble detachment characteristics. Therefore, it can be
881 concluded that the accurate measurement of the temperature value in the vicinity of the
882 generated bubbles is quite crucial for the numerical reproduction of experimental results on
883 nucleate boiling.

884 • For all three of the examined working fluids, both the bubble detachment time as well as the
885 equivalent bubble detachment diameter, decrease with the corresponding increase on the
886 applied gravitational acceleration, following a power law. It is quite important that this power
887 law effect on the bubble detachment characteristics, almost disappears at pressure conditions
888 higher than atmospheric. This constitutes a quite useful finding for the design of experimental
889 setups for microgravity and hyper gravity experiments and therefore it worth to further
890 investigate the bubble detachment characteristics for a variety of different pressure levels below
891 and above atmospheric pressure, for the same gravitational acceleration values as the ones
892 considered here.

893 • It is also interesting in general that, the influence of all of the examined controlling parameters,
894 is higher in the bubble detachment time in comparison to the bubble detachment diameter.

895 • In comparison, the overall results of the present parametric analysis indicate that the bubble
896 detachment characteristics are more affected by the heated plate Superheat, among the overall
897 examined controlling parameters. The ITBL thickness and the heated surface wettability (contact
898 angle) are the next in turn influential parameters, while the less influential parameter is the
899 applied gravitational acceleration. However, further investigations need to be conducted here,
900 considering the relative effect of gravity level at lower superheats and pressure conditions that
901 the ones considered, in the present parametric analysis.
902
903 Summarizing, the present investigation adds significantly to the existing knowledge on bubble
904 growth and detachment, in cases of saturated pool boiling of refrigerants, since a comprehensive
905 examination of the effect of fundamental controlling parameters on the bubble detachment
906 characteristics is conducted (more than 100, high resolution, transient, numerical simulations were
907 conducted for the purposes of the present investigation), identifying their exact quantitative influence
908 on the bubble detachment diameter and time as well as their relative importance. Finally, it can be
909 said that the use of the improved VOF-based interface capturing approach that is proposed,
910 presented, validated and applied in the present investigation, constitutes a quite promising and novel
911 tool for the simulation of bubble growth and detachment processes, providing great insight regarding
912 the complex underlined physics, hydrodynamics and thermodynamics, of such two-phase flow
913 phenomena of significant interest to real technological applications.

914 **A**cknowledgments: Part of the results presented in the present paper, constitute part of a wider research work,
915 which was related to the development of a VOF-based flow boiling model, able to predict the bubble detachment
916 characteristics in cases of diesel fuel flow boiling within injector nozzles, and it has received funding from the
917 People Programme (IAPP Marie Curie Actions) of the European Union's Seventh Framework Programme
918 FP7/2007-2013/ under REA grant agreement n. 324313. The authors would also like to acknowledge the
919 contribution of the super-computing facilities of CINECA, in Bologna (Italy), for the conduction of the large
920 number of numerical simulations of the present investigation, in a relatively short time. Part of the present work
921 has also been carried forward in the framework of the ESA MAP Project INWIP. Therefore, the authors would
922 also like to thank Dr. Olivier Minster and Dr. Balazs Toth, for their interest and support.

923 ## References

924 1. Nelson, R. A. Do we doubt too little? Examples from the thermal sciences. *Exp. Therm. Fluid Sci.* **2001**, *25*, 255–267.

925 2. Jakob, M.; Fritz, W. Versuche über den Verdampfungsvorgang. *Forsch. auf dem Gebiet der Ingenieurwissenschaften*
926 **1931**, *2*, 435–447.
927 3. Fritz, W. Berechnung des Maximalvolumens von Dampfblasen. *Phys. Zeitschrift* **1935**, *36*, 379–384.
928 4. Nukiyama, S. The maximum and minimum values of the heat Q transmitted from metal to boiling water under
929 atmospheric pressure. *Int. J. Heat Mass Transf.* **1966**, *9*, 1419–1433.
930 5. Zuber, N. Nucleate boiling. The region of isolated bubbles and the similarity with natural convection. *Int. J. Heat Mass*
931 *Transf.* **1963**, *6*, 53–78.
932 6. Cole, R. Bubble frequencies and departure volumes at subatmospheric pressures. *AIChE J.* **1967**, *13*, 779–783.
933 7. Malenkov, I. G. Detachment frequency as a function of size for vapor bubbles. *J. Eng. Phys.* **1971**, *20*, 704–708.
934 8. Stephan, K.; Abdelsalam, M. Heat-transfer correlations for natural convection boiling. *Int. J. Heat Mass Transf.* **1980**,
935 *23*, 73–87.
936 9. Carey, V. P. *Liquid Vapor Phase Change Phenomena: An Introduction to the Thermophysics of Vaporization and*
937 *Condensation Processes in Heat Transfer Equipment, Second Edition*; Taylor & Francis, 2007; Vol. 19.
938 10. Kenning, D. B. .; Kono, T.; Wienecke, M. Investigation of boiling heat transfer by liquid crystal thermography. *Exp.*
939 *Therm. Fluid Sci.* **2001**, *25*, 219–229.
940 11. Sodtke, C.; Kern, J.; Schweizer, N.; Stephan, P. High resolution measurements of wall temperature distribution
941 underneath a single vapour bubble under low gravity conditions. *Int. J. Heat Mass Transf.* **2006**, *49*, 1100–1106.
942 12. Wagner, E.; Sodtke, C.; Schweizer, N.; Stephan, P. Experimental study of nucleate boiling heat transfer under low
943 gravity conditions using TLCs for high resolution temperature measurements. *Heat Mass Transf.* **2006**, *42*, 875–883.
944 13. Baldassari, C.; Mameli, M.; Marengo, M. Non-Uniform Onset of Nucleate Flow Boiling of R-134a Inside a Glass
945 Minichannel. *Exp. Heat Transf.* **2014**, *27*, 316–328.
946 14. Jung, S.; Kim, H. An experimental method to simultaneously measure the dynamics and heat transfer associated with a
947 single bubble during nucleate boiling on a horizontal surface. *Int. J. Heat Mass Transf.* **2014**, *73*, 365–375.
948 15. Duan, X.; Phillips, B.; McKrell, T.; Buongiorno, J. Synchronized High-Speed Video, Infrared Thermometry, and Particle
949 Image Velocimetry Data for Validation of Interface-Tracking Simulations of Nucleate Boiling Phenomena. *Exp. Heat*
950 *Transf.* **2013**, *26*, 169–197.
951 16. Hassan, Y. A.; Estrada-Perez, C. E.; Yoo, J. S. Measurement of subcooled flow boiling using Particle Tracking
952 Velocimetry and infrared thermographic technique. *Nucl. Eng. Des.* **2014**, *268*, 185–190.
953 17. Demiray, F.; Kim, J. Microscale heat transfer measurements during pool boiling of FC-72: effect of subcooling. *Int. J.*
954 *Heat Mass Transf.* **2004**, *47*, 3257–3268.
955 18. Myers, J. G.; Yerramilli, V. K.; Hussey, S. W.; Yee, G. F.; Kim, J. Time and space resolved wall temperature and heat
956 flux measurements during nucleate boiling with constant heat flux boundary conditions. *Int. J. Heat Mass Transf.* **2005**, *48*,
957 2429–2442.
958 19. Moghaddam, S.; Kiger, K. Physical mechanisms of heat transfer during single bubble nucleate boiling of FC-72 under
959 saturation conditions-I. Experimental investigation. *Int. J. Heat Mass Transf.* **2009**, *52*, 1284–1294.
960 20. Delgoshaei, P.; Kim, J. Microscale Heat Transfer Measurements During Subcooled Pool Boiling of Pentane: Effect of
961 Bubble Dynamics. In *14th International Heat Transfer Conference*; ASME Digital COllection: Wshington, DC, **2010**; pp.
962 397–405.
963 21. Wagner, E.; Stephan, P.; Koeppen, O.; Auracher, H. High resolution temperature measurements at moving vapor/liquid
964 and vapor/liquid/solid interfaces during bubble growth in nucleate boiling. *Fortschr.-Ber. VDI* **2007**, *3*, 260–277.
965 22. Sempértegui, D.; Ribatski, G. Micro-Scale Flow Pattern Classification Based on the K-Means Clustering Algorithm. In
966 *ASME 2010 8th International Conference on Nanochannels, Microchannels, and Minichannels collocated with 3rd Joint*
967 *US-European Fluids Engineering Summer Meeting*; Montreal, Quebec, Canada, 2010; pp. 1619–1627.
968 23. Kurul, N.; Podowski, M. Z. Multidimensional effects in forced convection subcooled boiling. In *9th International Heat*

969 *Transfer Conference*; 1990; pp. 19–24.
970 24. Steiner, H.; Kobor, A.; Gebhard, L. A wall heat transfer model for subcooled boiling flow. *Int. J. Heat Mass Transf.*
971 **2005**, *48*, 4161–4173.
972 25. Koncar, B.; Krepper, E. CFD simulation of forced convective boiling in heated channels. **2007**.
973 26. Lopez-de-Bertodano, M. A.; Prabhudharwadkar, D. CFD Two Fluid Model for Adiabatic and Boiling Bubbly Flows in
974 Ducts. In *Computational Fluid Dynamics (INTECH)*; Hyoung Woo Oh, Ed.; 2010; pp. 29–52.
975 27. Yun, B.-J.; Splawski, A.; Lo, S.; Song, C.-H. Prediction of a subcooled boiling flow with advanced two-phase flow
976 models. *Nucl. Eng. Des.* **2012**, *253*, 351–359.
977 28. Krepper, E.; Rzehak, R.; Lifante, C.; Frank, T. CFD for subcooled flow boiling: Coupling wall boiling and population
978 balance models. *Nucl. Eng. Des.* **2013**, *255*, 330–346.
979 29. Prabhudharwadkar, D.; Lopez-de-Bertodano, M. A.; Hibiki, T.; Buchanan, J. R. Assessment of subcooled boiling wall
980 boundary correlations for two-fluid model CFD. *Int. J. Heat Mass Transf.* **2014**, *79*, 602–617.
981 30. Cheung, S. C. P.; Vahaji, S.; Yeoh, G. H.; Tu, J. Y. Modeling subcooled flow boiling in vertical channels at low pressures
982 – Part 1: Assessment of empirical correlations. *Int. J. Heat Mass Transf.* **2014**, *75*, 736–753.
983 31. Harlow, F. H.; Welch, J. E. Numerical Calculation of Time-Dependent Viscous Incompressible Flow of Fluid with Free
984 Surface. *Phys. Fluids* **1965**, *8*, 2182.
985 32. Tryggvason, G.; Bunner, B.; Esmaeeli, A.; Juric, D.; Al-Rawahi, N.; Tauber, W.; Han, J.; Nas, S.; Jan, Y.-J. A Front-
986 tracking Method for the Computations of Multiphase Flow. *J. Comput. Phys.* **2001**, *169*, 708–759.
987 33. Hirt, C. .; Amsden, A. .; Cook, J. . An arbitrary Lagrangian-Eulerian computing method for all flow speeds. *J. Comput.*
988 *Phys.* **1974**, *14*, 227–253.
989 34. Hirt, C. .; Nichols, B. . Volume of fluid (VOF) method for the dynamics of free boundaries. *J. Comput. Phys.* **1981**, *39*,
990 201–225.
991 35. Osher, S.; Sethian, J. A. Fronts propagating with curvature-dependent speed: Algorithms based on Hamilton-Jacobi
992 formulations. *J. Comput. Phys.* **1988**, *79*, 12–49.
993 36. Madhavan, S.; Mesler, R. B. A study of vapor bubble growth on surfaces. In *International Heat Transfer Conference 4*;
994 **1970**; pp. 1–11.
995 37. Glimm, J.; Grove, J.; Lindquist, B.; McBryan, O. A.; Tryggvason, G. The Bifurcation of Tracked Scalar Waves. *SIAM*
996 *J. Sci. Stat. Comput.* **1988**, *9*, 61–79.
997 38. Unverdi, S. O.; Tryggvason, G. A front-tracking method for viscous, incompressible, multi-fluid flows. *J. Comput. Phys.*
998 **1992**, *100*, 25–37.
999 39. Juric, D.; Tryggvason, G. Computations of boiling flows. *Int. J. Multiph. Flow* **1998**, *24*, 387–410.
1000 40. Esmaeeli, A.; Tryggvason, G. Computations of film boiling. Part I: numerical method. *Int. J. Heat Mass Transf.* **2004**,
1001 *47*, 5451–5461.
1002 41. Esmaeeli, A.; Tryggvason, G. Computations of film boiling. Part II: multi-mode film boiling. *Int. J. Heat Mass Transf.*
1003 **2004**, *47*, 5463–5476.
1004 42. Esmaeeli, A.; Tryggvason, G. A front tracking method for computations of boiling in complex geometries. *Int. J.*
1005 *Multiph. Flow* **2004**, *30*, 1037–1050.
1006 43. Welch, S. W. J. Local Simulation of Two-Phase Flows Including Interface Tracking with Mass Transfer. *J. Comput.*
1007 *Phys.* **1995**, *121*, 142–154.
1008 44. Welch, S. W. J. Direct simulation of vapor bubble growth. *Int. J. Heat Mass Transf.* **1998**, *41*, 1655–1666.
1009 45. Fuchs, T.; Kern, J.; Stephan, P. A Transient Nucleate Boiling Model Including Microscale Effects and Wall Heat
1010 Transfer. *J. Heat Transfer* **2006**, *128*, 1257–1265.
1011 46. Kern, J.; Stephan, P. Investigation of Decisive Mixture Effects in Nucleate Boiling of Binary Mixtures Using a
1012 Theoretical Model. *J. Heat Transfer* **2003**, *125*, 1116–1122.

1013 47. Kern, J.; Stephan, P. Theoretical Model for Nucleate Boiling Heat and Mass Transfer of Binary Mixtures. *J. Heat*
1014 *Transfer* **2003**, *125*, 1106–1115.
1015 48. Welch, S. W. J.; Wilson, J. A Volume of Fluid Based Method for Fluid Flows with Phase Change. *J. Comput. Phys.*
1016 **2000**, *160*, 662–682.
1017 49. Welch, S. W. J.; Rachidi, T. Numerical computation of film boiling including conjugate heat transfer. *Numer. Heat*
1018 *Transf. Part B Fundam.* **2002**, *42*, 35–53.
1019 50. Wiesche, S. aus der Bubble growth and departure during nucleate boiling: the occurrence of heat flux reversal. **2005**.
1020 51. Hardt, S.; Wondra, F. Evaporation model for interfacial flows based on a continuum-field representation of the source
1021 terms. *J. Comput. Phys.* **2008**, *227*, 5871–5895.
1022 52. Kunugi, T.; Saito, N.; Fujita, Y.; Serizawa, A. Direct numerical simulation of pool and forced convective flow boiling
1023 phenomena. *Heat Transf.* **2002**, *3*, 497–502.
1024 53. Ose, Y.; Kunugi, T. Numerical Study on Sabcooled Pool Boiling. *Prog. Nucl. Sci. Technol.* **2011**, *2*, 125–129.
1025 54. Ose, Y.; Kunugi, T. Development of A Boiling and Condensation Model on Subcooled Boiling Phenomena. *Energy*
1026 *Procedia* **2011**, *9*, 605–618.
1027 55. Pan, L.; Tan, Z.; Chen, D.; Xue, L. Numerical investigation of vapor bubble condensation characteristics of subcooled
1028 flow boiling in vertical rectangular channel. *Nucl. Eng. Des.* **2012**, *248*, 126–136.
1029 56. Jeon, S.-S.; Kim, S.-J.; Park, G.-C. Numerical study of condensing bubble in subcooled boiling flow using volume of
1030 fluid model. *Chem. Eng. Sci.* **2011**, *66*, 5899–5909.
1031 57. Kunkelmann, C.; Ibrahem, K.; Schweizer, N.; Herbert, S.; Stephan, P.; Gambaryan-Roisman, T. The effect of three-
1032 phase contact line speed on local evaporative heat transfer: Experimental and numerical investigations. *Int. J. Heat Mass*
1033 *Transf.* **2012**, *55*, 1896–1904.
1034 58. Kunkelmann, C.; Stephan, P. CFD Simulation of Boiling Flows Using the Volume-of-Fluid Method within OpenFOAM.
1035 *Numer. Heat Transf. Part A Appl.* **2009**, *56*, 631–646.
1036 59. Kunkelmann, C. Numerical Modeling and Investigation of Boiling Phenomena. phdthesis, Technische Universität:
1037 Darmstadt, **2011**.
1038 60. Son, G.; Dhir, V. K. Numerical Simulation of Film Boiling Near Critical Pressures With a Level Set Method. *J. Heat*
1039 *Transfer* **1998**, *120*, 183–192.
1040 61. Son, G.; Dhir, V. K.; Ramanujapu, N. Dynamics and Heat Transfer Associated With a Single Bubble During Nucleate
1041 Boiling on a Horizontal Surface. *J. Heat Transfer* **1999**, *121*, 623–631.
1042 62. Dhir, V. K. Numerical simulations of pool-boiling heat transfer. *AIChE J.* **2001**, *47*, 813–834.
1043 63. Lee, W.; Son, G.; Yoon, H. Y. Numerical study of bubble growth and boiling heat transfer on a microfinned surface.
1044 *Int. Commun. Heat Mass Transf.* **2012**, *39*, 52–57.
1045 64. Shu, B.; Ingenieure., V. D. Numerische Simulation des Blasensiedens mit Volume-Of-Fluid- und Level-Set-Methode.
1046 THES, VDI Verlag: Dusseldorf, 2010.
1047 65. Hazi, G.; Markus, A. On the bubble departure diameter and release frequency based on numerical simulation results.
1048 *Int. J. Heat Mass Transf.* **2009**, *52*, 1472–1480.
1049 66. Badillo, A. Quantitative phase-field modeling for boiling phenomena. *Phys. Rev. E. Stat. Nonlin. Soft Matter Phys.* **2012**,
1050 *86*, 41603.
1051 67. Georgoulas, A.; Koukouvinis, P.; Gavaises, M.; Marengo, M. Numerical investigation of quasi-static bubble growth and
1052 detachment from submerged orifices in isothermal liquid pools: The effect of varying fluid properties and gravity levels.
1053 *Int. J. Multiph. Flow* **2015**, *74*, 59–78.
1054 68. Magnini, M.; Pulvirenti, B. Height function interface reconstruction algorithm for the simulation of boiling flows. In
1055 *WIT Transactions on Engineering Sciences*; WIT Press, **2011**; Vol. 70, pp. 69–80.
1056 69. Lee, H. C.; Oh, B. Do; Bae, S. W.; Kim, M. H. Single bubble growth in saturated pool boiling on a constant wall

1057 temperature surface. *Int. J. Multiph. Flow* **2003**, *29*, 1857–1874.
1058 70. Brackbill, J. .; Kothe, D. .; Zemach, C. A continuum method for modeling surface tension. *J. Comput. Phys.* **1992**, *100*,
1059 335–354.
1060 71. Hoang, D. A.; van Steijn, V.; Portela, L. M.; Kreutzer, M. T.; Kleijn, C. R. Benchmark numerical simulations of
1061 segmented two-phase flows in microchannels using the Volume of Fluid method. *Comput. Fluids* **2013**, *86*, 28–36.
1062 72. Deshpande, S. S.; Anumolu, L.; Trujillo, M. F. Evaluating the performance of the two-phase flow solver interFoam.
1063 *Comput. Sci. Discov.* **2012**, *5*, 14016.
1064 73. OpenFOAM, The Open Source CFD Toolbox, User Guide. **2013**.
1065 74. Scardovelli, R.; Zaleski, S. Direct Numerical Simulation of Free-Surface and Interfacial Flow. *Annu. Rev. Fluid Mech.*
1066 **1999**, *31*, 567–603.
1067 75. Schrage, R. W. A theoretical study of interphase mass transfer. THES, Columbia University Press: New York, **1953**.
1068 76. Kunkelmann, C.; Stephan, P. Numerical simulation of the transient heat transfer during nucleate boiling of refrigerant
1069 HFE-7100. *Int. J. Refrig.* **2010**, *33*, 1221–1228.
1070 77. Kunkelmann, C.; Stephan, P. Modification and extension of a standard volume-of-fluid solver for simulating boiling
1071 heat transfer. In *Proceedings ECCOMAS CFD 2010 {--} Fifth European Conference on Computational Fluid Dynamics*;
1072 **2010**.
1073 78. Magnini, M. CFD Modeling of Two-Phase Boiling Flows in the Slug Flow Regime with an Interface Capturing
1074 Technique, University of Bologna, **2012**.
1075 79. Plesset, M. S.; Zwick, S. A. The Growth of Vapor Bubbles in Superheated Liquids. *J. Appl. Phys.* **1954**, *25*, 493.
1076 80. Scriven, L. E. On the dynamics of phase growth: L. E. Scriven, Chem. Engng. Sci.10: 1–13, 1959. *Chem. Eng. Sci.*
1077 **1995**, *50*, 3905.
1078 81. Mukherjee, A.; Kandlikar, S. G. Numerical study of single bubbles with dynamic contact angle during nucleate pool
1079 boiling. *Int. J. Heat Mass Transf.* **2007**, *50*, 127–138.
1080 82. Gong, S.; Cheng, P. Numerical simulation of pool boiling heat transfer on smooth surfaces with mixed wettability by
1081 lattice Boltzmann method. *Int. J. Heat Mass Transf.* **2015**, *80*, 206–216.
1082 83. Liao, J.; Mei, R.; Klausner, J. F. The influence of the bulk liquid thermal boundary layer on saturated nucleate boiling.
1083 *Int. J. Heat Fluid Flow* **2004**, *25*, 196–208.
1084 84. Dhir, V. K. Mechanistic Prediction of Nucleate Boiling Heat Transfer–Achievable or a Hopeless Task? *J. Heat Transfer*
1085 **2005**, *128*, 1–12.
1086 85. Bourdon, B.; Rioboo, R.; Marengo, M.; Gosselin, E.; De Coninck, J. Influence of the Wettability on the Boiling Onset.
1087 *Langmuir* **2012**, *28*, 1618–1624.
1088 86. Bourdon, B.; Bertrand, E.; Di Marco, P.; Marengo, M.; Rioboo, R.; De Coninck, J. Wettability influence on the onset
1089 temperature of pool boiling: Experimental evidence onto ultra-smooth surfaces. *Adv. Colloid Interface Sci.* **2015**, *221*, 34–
1090 40.
1091 87. Nam, Y.; Wu, J.; Warrier, G.; Ju, Y. S. Experimental and Numerical Study of Single Bubble Dynamics on a Hydrophobic
1092 Surface. *J. Heat Transfer* **2009**, *131*, 121004.
1093 88. Malavasi, I.; Bourdon, B.; Di Marco, P.; de Coninck, J.; Marengo, M. Appearance of a low superheat "quasi-Leidenfrost"
1094 regime for boiling on superhydrophobic surfaces. *Int. Commun. Heat Mass Transf.* **2015**, *63*, 1–7.
1095 89. Sanna, A. Numerical investigation of saturated flow boiling on thin walls, **2010**.
1096